# FLUX PINNING IN SUPERCONDUCTING Nb-Ti WIRES

# WITH Nb ARTIFICIAL PINNING CENTERS

by

Robert W. Heussner

A dissertation submitted in partial fulfillment

of the requirements for the degree of

Doctor of Philosophy

(Materials Science)

at the

UNIVERSITY OF WISCONSIN - MADISON

1998

# Acknowledgments

I thank my advisor, Professor David Larbalestier, for providing me with many opportunities, encouragement, and guidance over the years for which I am truly grateful. I also appreciate the help and friendship of the entire Superconducting Materials Research Group, who made my time at UW enjoyable.

In particular, I thank: Paul Jablonski, for teaching me the fine art of composite wire manufacture, and whose own work provided a basis for this thesis; Lance Cooley, for his close collaboration throughout this work; Peter Lee, for performing painstaking TEM on my wires; Cristina Bormio-Nunes, for providing electromagnetic characterization which complemented my own experimental results; and Alex Pashitski, Alex Gurevich, Jeff Parrell and Mike Naus, for helpful scientific discussions. I was also fortunate to work with several bright undergraduates, including Jesse Marquardt, Matt Schlinkert, and Matt Pelletier, who assisted in the fabrication and characterization of composite wires.

A special thanks is due to Bill Starch and Alex Squitieri who, in addition to maintaining our excellent fabrication and electromagnetic characterization facilities, were always willing to devote their time to this project. I also thank Mel Adams and Kim Bass, who deserve much credit for keeping the Center running smoothly. I thank my doctoral committee, particularly Professors Eric Hellstrom, Sue Babcock, Tom Kelly, and David for their excellent instruction throughout my materials science education.

Finally, I am indebted to my parents, Bob and Sarah, for their support in all the choices I have made. I am forever grateful to my wife, Wendy, for her love and encouragement.

# FLUX PINNING IN SUPERCONDUCTING Nb-Ti WIRES

# WITH Nb ARTIFICIAL PINNING CENTERS

Robert W. Heussner

Under the supervision of Professor David C. Larbalestier

At the University of Wisconsin-Madison

Superconducting Nb-Ti wires containing uniform arrays of round Nb artificial pinning centers were fabricated and their microstructures and electromagnetic properties characterized as the pin diameter and spacing were reduced to the nanometer dimensions of the flux line lattice. Through careful control of the thermomechanical treatment, the critical current density ($J_c$) of a composite containing Nb 47 wt.% Ti with 24 volume percent of Nb pins was raised to 4600 A/mm$^2$ at the benchmark field (5 T) and temperature (4.2 K), thus establishing a new record for any round wire of Nb-Ti. Maximum $J_c$(5 T) occurred for a nominal pin diameter ($d_p$) of 25 nm, but for which the actual pins were 1–15 nm thick elongated ribbons. Despite the extremely high $J_c$ values at low fields (1–6 T), the high-field $J_c$ (6–9 T) was depressed due to the combination of a proximity-effect depressed upper critical field, and a characteristic low-field maximum in the field-dependent pinning force density. A Nb 62 wt.% Ti-matrix composite, designed for maximum upper critical field in the coupled limit, exhibited an increased irreversibility field as the pin size was reduced. However, this enhancement was significantly less than

iv

predicted for the fully coupled limit, even when the pins were much thinner than the superconducting coherence length. In the context of existing proximity effect models, this can be attributed to the same minimal pin/matrix interdiffusion held responsible for high $J_c$ at low fields. Finally, through separate alloying additions of 7.5 wt.% Ta and 10 wt.% W, the Nb-pin proximity length ($x_N$) was reduced by 30% and 60%, respectively. The functional dependence of the pinning force density on $x_N$, $d_p$, and field agrees qualitatively with the magnetic pinning model of Cooley, Lee, and Larbalestier.

# Contents

# 1. Introduction

Niobium titanium is the most widely used superconductor. This is despite the existence

of other superconductors which possess higher critical temperatures ($T_c$) and critical

magnetic fields, most notably the A15 (e.g. $Nb_3Sn$), Chevrel phase (e.g. $PbMo_6S_8$) and

high-temperature copper-oxide (e.g. $Bi_2Sr_2CaCu_2O_8$ and $YBa_2Cu_3O_7$) ceramic

compounds. Nb-Ti is chosen because it is ductile, strong, and provides a technologically

useful critical current density ($J_c$>1 kA/mm$^2$) in fields up to ~8 T at 4.2 K and ~11 T at

1.8 K. High energy physics projects propel the investigation of ever greater high-field $J_c$

in Nb-Ti since particle accelerator magnets benefit from high $J_c$. Furthermore, mature

technologies such as magnetic resonance imaging, electric power conditioning, and

laboratory magnets benefit from all $J_c$ improvements. In bulk superconducting materials,

$J_c$ can be determined by a hierarchy of limiting mechanisms, but it is ultimately limited by

the pinning of the flux line lattice by the defect structure. Thus the key to raising $J_c$ lies

in controlling the defect structure and relating it to the flux pinning and other superconducting properties.

## 1.1  Flux pinning in type-II superconductors

Two distinct types of superconductors are characterized by their response to applied magnetic fields, as illustrated by the *H–T* phase diagrams of Figure 1.1.  To understand the origin of the difference in behavior requires a microscopic description of the superconducting properties.  All superconductors are characterized by two intrinsic length scales:  the magnetic penetration depth (*l*) [1], or the distance over which the magnetic field (*H*) can vary, and the coherence length (*x*) [2], or the distance over which the superconducting order parameter (*Y*) can vary.  The ratio of these two lengths, called the Ginzburg-Landau parameter (*k*) [3],

$$\kappa = \lambda/\xi \, , \tag{1.1}$$

determines whether the superconductor is type-I or type-II.  Type-I superconductors ($k < 1/\sqrt{2}$) have a positive interfacial energy between the normal and superconducting states, given approximately by $\frac{1}{2}\mu_0 H_c^2(\xi - \lambda)$ [4].  Thus complete flux exclusion, or a so-called *Meissner* state, [5] minimizes the interface energy.  This state persists up to the critical field ($H_c$) of order 10–100 mT.  At this point, the further increase in free energy due to flux exclusion exceeds the decrease in free energy associated with the superconducting state and the material returns to the normal state.
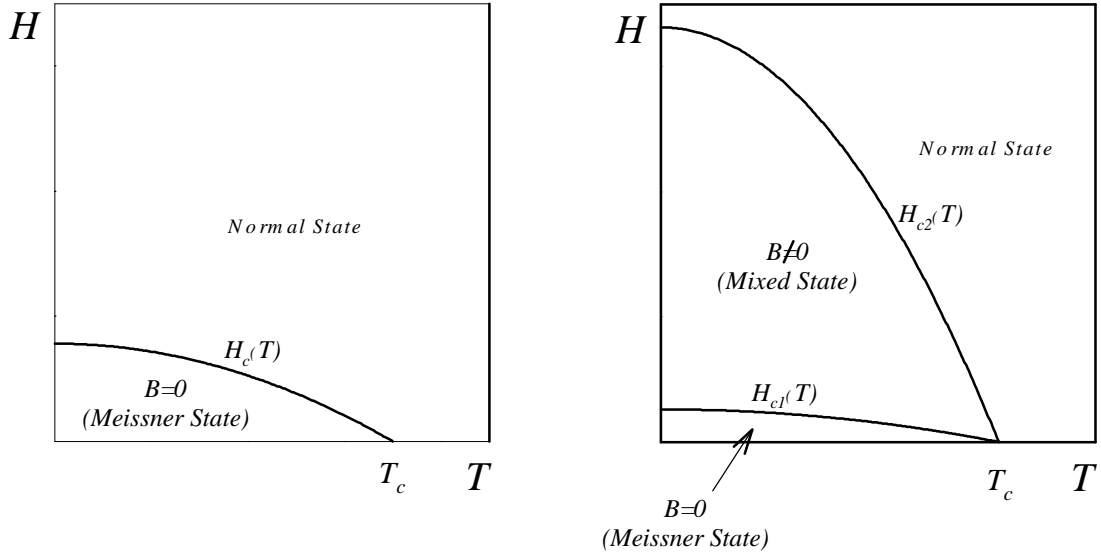
Figure 1.1: Schematic *H–T* phase diagrams for (a) type-I and (b) type-II superconductors.

Conversely, type-II superconductors $(k > 1/\sqrt{2})$ have a negative normal–superconductor interfacial energy and thus flux inclusion becomes energetically favorable above a lower critical field ($H_{c1}$). In order to maximize the contribution of interface energy, flux penetrates the superconductor in many discrete flux quanta or *fluxons*, each fluxon containing a single flux quantum ($f_0$) given by:

$$\phi_0 = h/2e = 2.07 \times 10^{-15} \text{ Wb}. \tag{1.2}$$

The structure of a fluxon structure consists of a short-range (of order *x*) normal core surrounded by a long-range (of order *l*) vortex of supercurrent. As the field is increased further beyond $H_{c1}$, the density of fluxons increases, and fluxon–fluxon repulsion leads to

the formation of a hexagonal flux line lattice (FLL) with spacing $a_0 = 1.07\sqrt{f_0/B}$ [6].

Eventually, the internal flux density ($B$) equals the applied flux density at the upper

critical field ($H_{c2}$) defined by

$$H_{c2}(T) = \kappa\sqrt{2}H_c(T) = \phi_0/2\pi\mu_0\xi(T)^2 .\qquad (1.3)$$

The region of the $H$–$T$ phase diagram between $H_{c1}$ and $H_{c2}$ (Figure 1.1b) is referred to as

the *mixed* (or vortex) state.  All technologically useful superconducting materials are

type II because current is carried throughout the bulk and because the upper critical field

is much higher (of order T versus mT) than type I.  Therefore, the remainder of this

chapter focuses on fluxon–defect and fluxon–fluxon interactions in type-II

superconductors.

### 1.1.1  Elementary pinning force

In the presence of a transport current density ($J$), the FLL of a type-II superconductor in

the mixed state experiences a bulk Lorentz force $\mathbf{F_L} = \mathbf{J} \times \mathbf{B}$.  A schematic of this

situation is shown in Figure 1.2 for a slab of type-II superconductor  If left unbalanced,

the Lorentz force will move the fluxon cores, leading to energy dissipation and electrical

resistance.  However, fluxons are easily *pinned* by regions of weaker superconductivity,

such as a microstructural defects.  A vector sum of these elementary pinning forces ($f_p$)

balances the Lorentz force.

$F_L \rightarrow \; \leftarrow F_p$

$H$

$J$  $J$
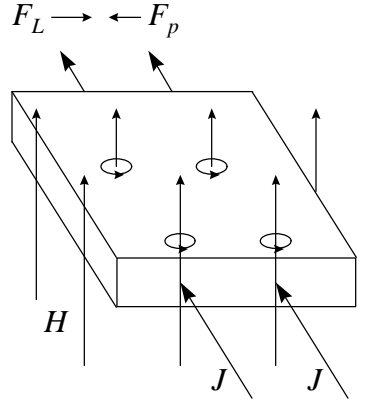
Figure 1.2: Force balance between the bulk pinning force $F_p$ and the Lorentz force $F_L$ which defines the critical state and $J_c$. The orientations of $J$, $H$, $F_L$, and $F_p$ are shown for a slab geometry.

Several mechanisms can give rise to an elementary pinning force. The normal core of

a fluxon is associated with a condensation energy density of order $\mathbf{m}_0 H_c^2$ [7]. If the core

is located on a defect where the superconducting order parameter is locally depressed,

some or all of the condensation energy can be recovered. This is referred to as the *core*

*interaction*. For the simplest case of an isolated fluxon located over a void of diameter <

$\mathbf{x}$, the energy penalty of the core is reduced by $\frac{1}{2}\mu_0 H_c^2 V$, where $V$ is the volume of the

void. Dividing this energy by the characteristic distance over which $\mathbf{Y}$ varies gives a

rough estimate of the elementary pinning interaction:

$$f_p = (V/2\xi)\mu_0 H_c^2 . \tag{1.4}$$

At finite reduced fields ($h \equiv H/H_{c2}$), the superconducting order parameter is reduced by a

factor of $(1-h)$, yielding a field-dependent elementary pinning force:

$$f_p(h) = (V/2\xi)\mu_0 H_c^2(1-h). \qquad (1.5)$$

However, voids are not practical pinning centers; non-superconducting precipitates are usually encountered in practice. Kramer and Freyhardt [8] calculated the elementary pinning force of a small (~$x$) proximity-effect coupled precipitate to be several orders of magnitude lower than for a void of similar size. However, Matsushita [9] argued that this analysis incorrectly treated the precipitate as a weak superconductor. Through application of the phenomenological Ginzburg–Landau theory, Matsushita found that $f_p$ of a coupled pin was approximately the *same* as that for a void. In support of this theory, measurements of the specific pinning force (average elementary pinning force) for normal-state $a$-Ti precipitates in conventionally processed Nb-Ti [10] were within a factor of 3 of the theory, with suitable allowance for the shape of the precipitate. In addition, flux pinning calculations by Stejic [11] for a simulated Nb-Ti microstructure support the hypothesis of Matsushita.

In addition to core pinning, long-range distortion of the vortex supercurrent by defects produces a magnetic pinning interaction. The magnetic pinning force can be calculated by determining the vortex current configuration in the London approximation [7, 12, 13]. Since the energy associated with the supercurrent is of the same order of magnitude as the condensation energy associated with the core, magnetic pinning interactions can be as strong as core pinning interactions.

*1.1.2  Bulk pinning force*

Equations such as 1.5 can be used to determine the strength of the interaction between a single fluxon and a single pinning center.  However, since $J_c$ is determined by the *bulk* pinning force rather than by any single elementary pinning interaction, the process by which the elementary pinning forces are vectorially summed is very important.

Microscopically, the bulk pinning force ($F_p$) is determined by summation of the elementary pinning forces over the number density of pinning interactions ($N$):

$$\vec{F}_p = \sum_{i=1}^{N} \eta_i \vec{f}_{pi} \approx \eta f_p N . \tag{1.6}$$

A pinning efficiency factor **h** [14] is introduced to account for the geometrical distribution of pinning centers and the rigidity of the FLL.  If the FLL interaction is strong with respect to $f_p$, then $\eta \rightarrow 0$ and thus $F_p \rightarrow 0$.  Conversely, if the FLL interaction is much weaker than $f_p$, then **h** is determined by a geometrical factor related to the defect structure and $F_p$ is determined by direct summation of the elementary pinning forces.  Direct summation implies that $f_p$ can be multiplied by $N$ directly to give the bulk pinning force; this is expected to be a reasonable approximation for a system of strong pins with a spacing comparable to the FLL spacing.  For core pinning, $F_p(H) \propto h(1-h)$ as follows from Equation 1.3 and the expectation that $N \propto h$.

The derivation of $F_p$ from microscopic quantities using Equation 1.6 requires a thorough understanding of the pinning mechanism(s) and a quantitative description of the defect structure.  In most cases, neither of these are known with great certainty.  The

8

force balance requires that $F_p$ is determined by the product of the critical current density and the flux density:

$$\vec{F}_p = \vec{J}_c \times \vec{B}.$$ (1.7)

Note that when $H \gg H_{c1}$, $B \sim m_0 H$, so it is only necessary to know the applied field in order to find $F_p$.

Temperature scaling of the field-dependent bulk pinning force in high-$\boldsymbol{k}$ superconductors (such as Nb-Ti) was first reported by Fietz and Webb [15] and can be expressed as:

$$F_p = \left[H_{c2}(T)\right]^m f(h),$$ (1.8)

where $m$ is the scaling exponent. Scaling of $F_p(H)$ over a wide range of temperature is usually a good indication that one pinning mechanism is present. Temperature scaling has been observed in cold-worked Nb-Ti [10] and under certain conditions in optimized Nb-Ti [10]. A lack of temperature scaling is usually attributed to the presence of more than one type of pinning center or more than one type of pinning mechanism [7]. $f(h)$ generally takes the form of $h^p (1-h)^q$, where the exponents $p$ and $q$ depend on both the nature of the elementary pinning interaction and the elasticity of the flux line lattice [16]. Thus, measurements of the bulk pinning force as a function of field and temperature can be used to deduce information about the pinning mechanism(s) that operate [7, 12].
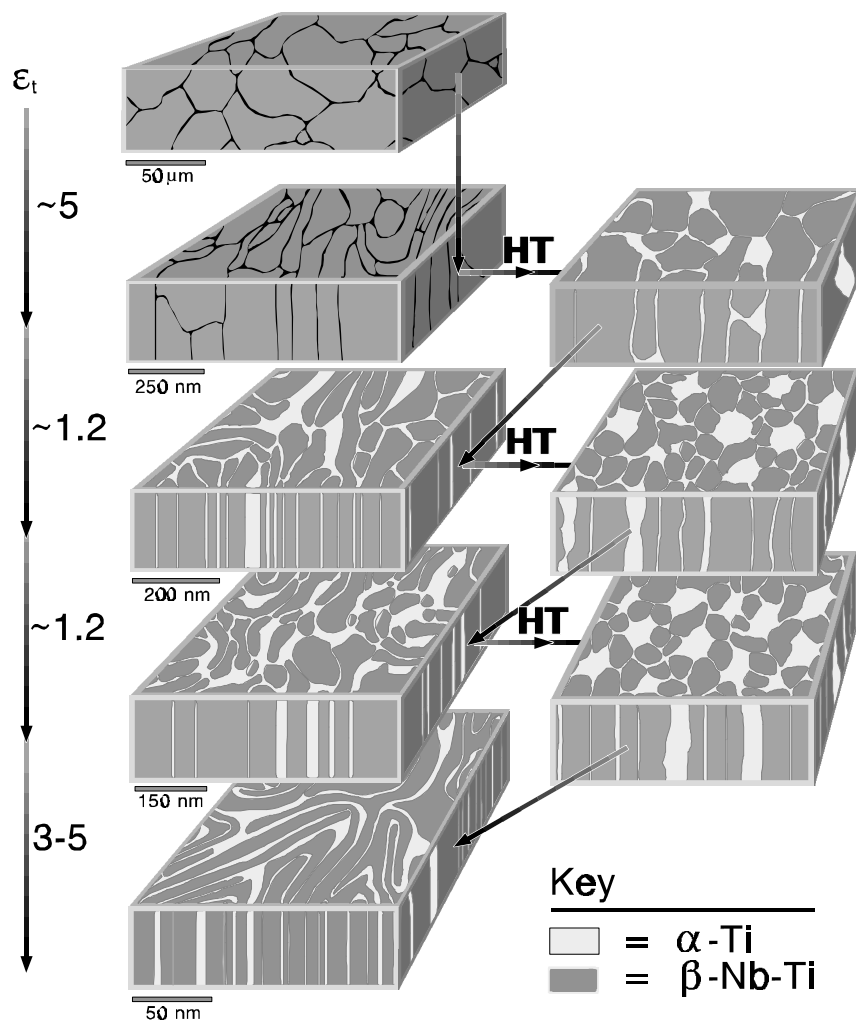
Figure 1.3: Schematic illustrating the development of a strong flux-pinning nanostructure in Nb-Ti wire through conventional thermomechanical processing (courtesy of Dr. P.J. Lee).

## 1.2  Development of high-$J_c$ Nb-Ti wire

From the above discussion, an understanding of the flux pinning mechanism(s) in any strong pinning system such as Nb-Ti is clearly desirable.  However, the critical current density in Nb-Ti was, in fact, optimized *prior* to the development of a generally accepted flux pinning model.  $J_c$ optimization occurred primarily by means of microstructure– property correlations—the principle tenet of materials science.  Only *after* wires with high-$J_c$ were obtained (a situation corresponding to a high degree of both macro- and microstructural uniformity), *and* then only after wire microstructures were quantitatively characterized was a generally accepted flux-pinning model developed.

The key to increasing $J_c$ in Nb-Ti via conventional thermomechanical treatment came with the identification of non-superconducting *a*-Ti as the dominant, naturally occurring defect [17].  Obtaining high $J_c$ in Nb-Ti wire then became a matter of maximizing the precipitate volume fraction and refining the precipitate size and spacing to dimensions near those of the FLL.  Figure 1.3 schematically illustrates the thermomechanical processing steps and the microstructural development of a strong flux pinning nanostructure in Nb-Ti.  First, fabrication of high-$J_c$ Nb-Ti wire begins with high-homogeneity Nb 47 wt.% Ti alloy having a local chemical variation of less than 2 wt.%. [18]    Prior to *a*-Ti precipitation heat treatment, a minimum drawing strain $e = 2\ln(d_i / d_f)$ of 4 is required to develop a dense dislocation substructure.  This suppresses the formation of undesirable ω or Widmanstätten phase morphologies during heat treatment [19].  A series of heat treatment and drawing steps are used to nucleate
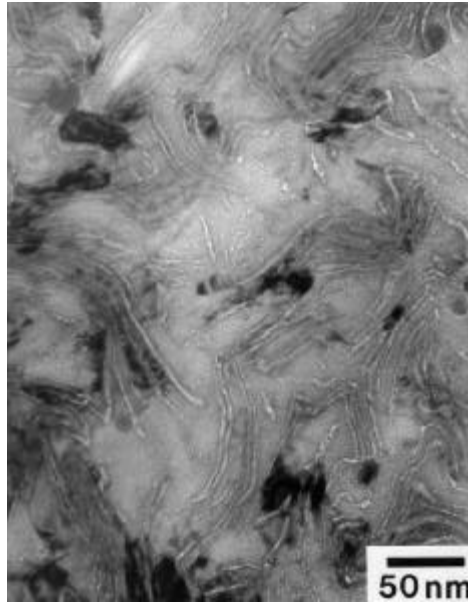
Figure 1.4: Transmission electron microscopy photograph of a conventionally processed Nb 48 wt.% Ti wire at optimum flux pinning diameter (transverse section). The thin light gray ribbons are *a*-Ti. The dark, approximately equiaxed regions are strongly diffracting *b*-Nb-Ti grains (Photo courtesy of Dr. P.J. Lee).

and grow up to 20–25 vol.% of 100–200 nm-diameter ellipsoid-shaped *a*-Ti precipitates [20, 21]. Generally 3 or 4 40–80 hr, 375–420°C heat treatments, each separated by a strain of one, are used for this purpose. A final drawing strain of ~5 refines the *a*-Ti precipitates into elongated ribbons with thickness and spacing near that of the superconducting coherence length (~5 nm for Nb 47 wt.% Ti at 4.2 K). A maximum bulk flux pinning force occurs when the ribbon thickness and spacing are 1–2 and 3–6 nm, respectively [22, 23] as shown by the transmission electron microscopy (TEM) image of optimized Nb 47 wt.% Ti wire in Figure 1.4.
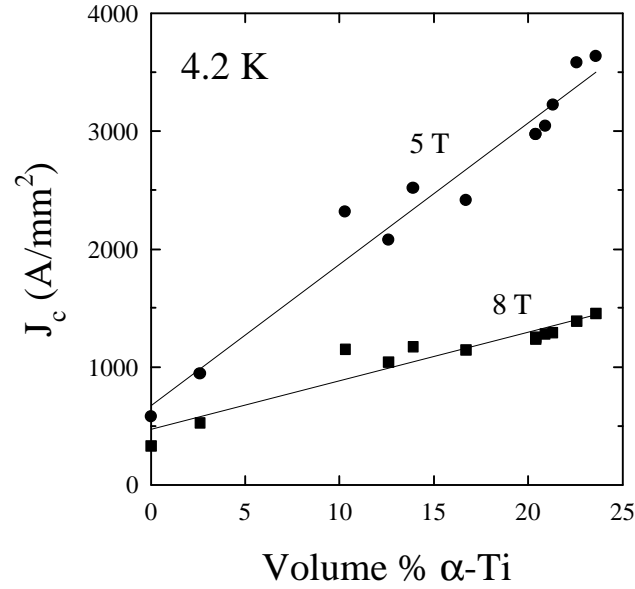
Figure 1.5: Critical current density at 5 and 8 T as a function of *a*-Ti volume fraction for conventionally processed Nb 47 wt.% Ti wire (Data courtesy of Dr. P.J. Lee).

As shown by Lee, McKinnell, and Larbalestier [24] in Figure 1.5, $J_c$ increases linearly with *a*-Ti volume fraction up to ~25%, the thermodynamic and/or kinetic limit for Nb 47 wt.% Ti. Numerical flux pinning simulations by Stejic et al. [25] predict a maximum $J_c$ (5 T) near 40 vol.%, if this can be achieved by other means.

## 1.3 Artificial pinning center wire

While the $J_c$ of Nb-Ti wire can be increased to technologically useful levels by conventional thermomechanical treatment, the maximum attainable $J_c$(5 T, 4.2 K) of 3700 A/mm$^2$ is still approximately fifty times lower than the depairing current density, the absolute limit on current density in a superconductor. Experimental [24] and

theoretical [25] predictions suggest that further increases in the volume fraction of $a$-Ti should lead to further increases in $J_c$. In addition, alternative pin materials and pin geometries may provide stronger elementary pinning interactions than the ribbon-shaped $a$-Ti precipitates.

One route to higher performance is to replace the precipitates with better pins. These so-called artificial pinning center (APC) superconductor designs do not suffer from thermodynamic or kinetic restrictions and thus offer greater flexibility in the choice of pinning center *composition*, *volume fraction*, and *arrangement*. Dorofejev et al. [26] first incorporated artificial pinning centers into Nb-Ti wires using a mechanical assembly technique, where the pinning centers were introduced as a starting component into the interior of the superconductor. Although a thorough characterization of the microstructure and superconducting properties was lacking, their pioneering study proved the principle and quickly generated interest within the low temperature superconductor community. Subsequent studies were initiated by Motowidlo et al. [27, 28], Cooley, Lee and Larbalestier [29, 30], Matsumoto et al. [31, 32, 33], and Wong et al. [34, 35]. While the choice of pin geometry varied, as shown in Figure 1.6, the fabrication methods used by each group are fundamentally the same. Each technique requires a starting pin size large enough, generally 1–10 mm, for easy handling. Consequently, very large strains of order 20–30 are required to reduce the artificial pinning centers to the nanometer dimensions of the FLL, twice the strain needed for
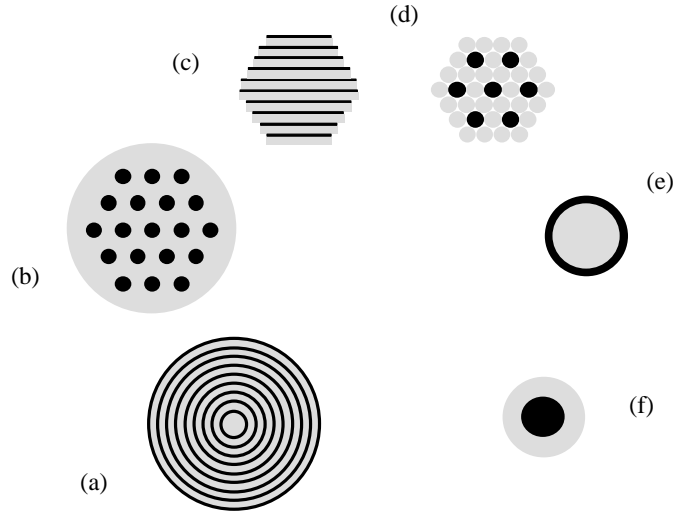
Figure 1.6:  Methods (strain intensive) used to incorporate artificial pinning centers into Nb-Ti wire:  (a) jelly roll [35], (b) gun-barrel-drilled [29], (c) multilayered planar [31], (d) rod-based [36, 37], (e) barrier-type [27], and (f) island-type [27].  In each case the pin is black and the Nb-Ti is gray.  The patterns shown represent the most primitive subdivision of each arrangement which defines the pin shape and volume fraction. Methods (a) and (b) are unique in that the pattern shown also defines the Nb-Ti filament cross section, while (c), (d), (e) and (f) are re-stacked together as bare elements to create a larger filament.  Methods (b), (d) and (e) produce equivalent round-pin arrays.

conventional processing (~12).  This is a serious economic handicap from a commercial manufacturing standpoint.

Jablonski and Larbalestier [38, 39] recognized that the total strain needed to fabricate APC composite wires could be reduced by a factor of 2 via powder metallurgy (PM) processing.  However, initial PMAPC wires containing Nb 55 wt.% Ti with 10–40 wt.% Nb [40, 41] achieved $J_c$ values of only half the level achieved in similar APC composites fabricated using other, strain-intensive techniques.  Detailed microstructural

analysis of PMAPC wires revealed that a broad distribution of pinning center thickness at optimum size was likely responsible for the depressed $J_c$ values. Presently, it is not known whether a broad distribution in pin thickness is intrinsic to the powder metallurgy process or is wholly due to characteristics of the starting powders.

A wide variety of APC compositions, fractions, and geometries have been used and some considerable successes have been achieved. A multilayered APC structure [33] consisting of Nb 50 wt.% Ti with 28 vol.% of Nb achieved 4250 A/mm$^2$ (5 T, 4.2 K), the highest value ever reported (prior to this thesis) for a round Nb-Ti wire. This high value was achieved despite the fact that the composite $H_{c2}$ was ~1 T less than that of Nb 47 wt.% Ti. However, present APC designs have some drawbacks, not the least of which results from the operation of the proximity effect [42, 43, 44, 45, 46].

### 1.3.1  Proximity-effect depression of $T_c$, $H_{c2}$

Most APC designs use Nb 47-50 wt.% Ti with 20-30 vol.% of Nb pins. At wire diameters which give optimum $J_c$, the pin thickness is sufficiently small for proximity-effect coupling to occur. Proximity-effect coupling of the pins to the matrix effectively homogenizes the values of $H_{c2}$ and $T_c$, changing them from values of the matrix composition to values representing a composite average [23]. In the case of Nb pins coupled to Nb 47 wt.% Ti, a Nb-rich overall composition results. The homogenized state should have a slightly higher $T_c$ but a considerably reduced $H_{c2}$, as illustrated by the plots of $T_c$ and $H_{c2}$ versus composition in Figure 1.7 [23, 47]. Other pin materials, such as Cu [48, 49], can reduce both $T_c$ and $H_{c2}$ in even more marked fashion. Proximity-
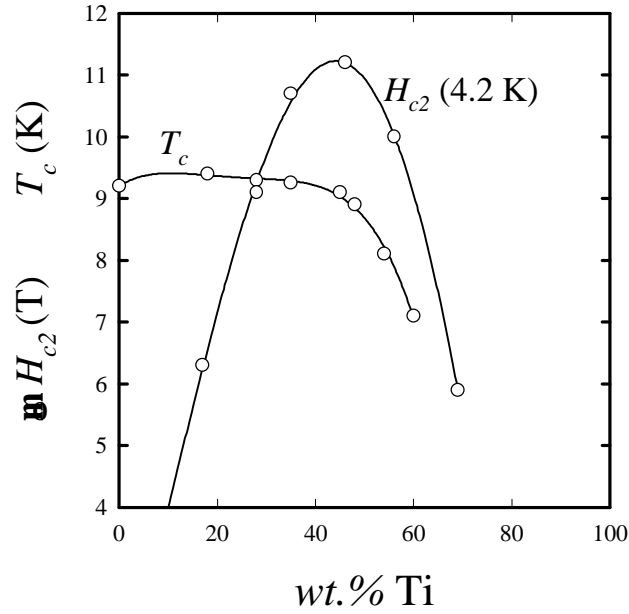
Figure 1.7: Critical temperature [23] and upper critical field at 4.2 K [47] as a function of Nb-Ti composition.

effect coupling also occurs in conventional Nb-Ti where the *a*-Ti precipitates are coupled to the matrix with composition ~Nb 39 wt.% Ti, but in this case the overall composition is close to that which gives maximum $H_{c2}$. The proximity effect exerts a beneficial effect in the conventional wire, serving to restore the high $H_{c2}$ that was lost during the composition changes that accompany the precipitation heat treatments. So, the key to optimizing $H_{c2}$ in APC wires thus appears to be in avoiding an overall composition which departs significantly from Nb 44–48 wt.% Ti, where $H_{c2}$ reaches its peak. One goal of this thesis is to explicitly test the proximity mixing hypothesis above by fabricating Nb-pin APC composites designed for maximum $H_{c2}$ in the fully coupled limit.

*1.3.2  The shape of $F_p(H)$*

Another important difference between APC and conventional wires lies in the shape of the bulk flux-pinning force curves.  In particular, the value of field at which the maximum pinning force ($F_{pmax}$) occurs is different.  Conventional composites exhibit a peak at ~$0.5H_{c2}$ while APC composites most often exhibit a peak at ~$0.25H_{c2}$.  Flux pinning in conventional Nb-Ti has long been explained with fluxon core pinning models [10], for which $F_{pmax}$~$0.5H_{c2}$ appears naturally, as argued previously.  This is seen experimentally, as shown in Figure 1.8, and the presence of a $h(1-h)$ shape of the bulk is thought to validate the core pinning hypothesis.  In addition, the $\boldsymbol{a}$-Ti precipitate number density far exceeds the number density of all other defects, and the functional dependence of $f_p$ derived from $F_p$ and the precipitate number density supports core pinning.  However, other data are not consistent with core pinning being the dominant mechanism.  For instance, the 1–4 nm thick $\boldsymbol{a}$-Ti ribbons at optimum size, are too thin to strongly interact with the 10 nm diameter fluxon cores at 4.2 K.  In addition, $F_p(H)$ data near $T_c$ yields $F_p \propto h^{1/2}(1-h)$ rather than the $h(1-h)$ functional dependence.

Since the nanostructure of APC composites is in fact very similar to that of conventional composites, the different behavior of $F_p(H)$ raised many questions.  In particular, the dominant pinning mechanism may be magnetic [50], rather than a core mechanism.  The importance of magnetic pinning interactions has recently been completely reevaluated [51] and a new model has been introduced to describe the behavior of both conventional and APC Nb-Ti.  Cooley, Lee, and Larbalestier [52, 53]
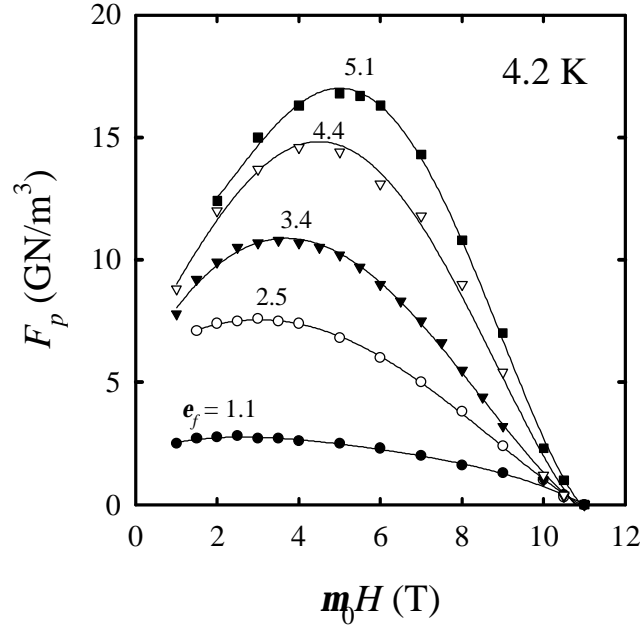
Figure 1.8: $F_p(H)$ as a function of final strain for conventionally processed Nb 48 wt.% Ti wire [10].

explain the difference in bulk pinning force curves between conventional and APC Nb-Ti as resulting from the different proximity lengths of pure Nb and *a*-Ti pins. This new model makes testable predictions of the optimum pin design for any Nb-Ti composite, and it proposes that APC Nb-Ti can be further advanced by reducing the electron mean free path of the pin. Thus a second goal of this thesis is to test the predictions of the magnetic pinning model.

## 1.4 Design of this thesis

This thesis follows two dissertations within our group on APC Nb-Ti wires. Cooley [29] studied a gun-barrel-drilled composite with the most uniform nanometer scale pinning

array to date, but for which the optimum $J_c$ properties were achieved when the superconducting filament diameter was of order $l$ (250 nm at 4.2 K). This sub-micron filament size produced an undesirably large surface pinning contribution to the bulk pinning force, thus complicating analysis of the pinning intrinsic to the pins. Jablonski [39] developed a novel powder metallurgy approach which reduced the fabrication strain needed to fabricate nanometer-scale pin arrays in wires by a factor of two. However the broad pin thickness distributions produced by this process were detrimental to $J_c$. Many of the lessons learned and techniques developed during the course of these two studies were effectively utilized in the present study. To first order, we sought to make APC composites with *large* ($>>l$) filament diameters and *uniform* pin arrays in order to circumvent the major obstacles encountered by Cooley and Jablonski. To this end, we were successful—many thanks to Lance and Paul!

The remainder of this thesis is framed around the design, fabrication and characterization of wires containing large ($>>l$) Nb-Ti filaments with uniform pinning centers arrays. The order follows a logical progression, beginning with a description of APC wire design, fabrication and characterization techniques in chapter 2, followed by a comprehensive study of the microstructure and properties of a preliminary composite containing Nb 47 wt.% Ti with 24 vol.% Nb pins in chapter 3. This initial study prompted three subsequent studies of more advanced composite designs described in chapters 4–6. Detailed descriptions of the remaining chapters follow.

Chapter 2 describes the design and fabrication of Nb-Ti wires with round artificial pinning centers and large ($>>l$) filament diameters. Composite wire design and fabrication issues related to monofilament and multifilament wire extrusion and drawing are discussed. In addition, the techniques used to measure the transport critical current density and magnetization are described.

Chapter 3 describes a comprehensive study of the microstructure and superconducting properties evolution of a preliminary APC composite containing Nb 47 wt.% Ti with 24 volume percent of round Nb pins. $J_c$, $F_p$, and the irreversibility field ($H^*$) are analyzed as the nominal pin diameter is reduced from 165 to 15 nm. A large discrepancy in $J_c(d_p, H)$ between composites which had received three or four warm ($650^{\circ}$C) in their fabrication was observed. The $J_c$ depression was attributed to pin–matrix interdiffusion caused by the fourth warm extrusion.

Chapter 4 discusses thermomechanical processing improvements designed to minimize pin–matrix interdiffusion, and thereby strengthen $f_p$. Accordingly, $J_c$ increased by 25–40% at all fields, rising from 3200 to 4600 A/mm$^2$ at the benchmark field (5 T) and temperature (4.2 K) and thus establishing a new high $J_c$ for round-wire Nb-Ti. However, just as in the earlier composite, the improved composite suffered from depressed $J_c$ at high-field for which two sources were identified: (**1**) $H_{c2}$ depression caused by the matrix composition not being optimized for maximum $H_{c2}$ in the fully coupled limit, and (**2**) a low-field maximum in $F_p(H)$, as predicted by the magnetic

pinning model of Cooley, Lee and Larbalestier for short proximity length pins such as Nb. Chapters 5 and 6 address each issue independently.

Chapter 5 addresses the proximity-effect depression of $H_{c2}$ and $T_c$ observed in all existing Nb-pin APC composites. In order to design for maximum $H_{c2}$ and $T_c$, the starting Ti content of the matrix was increased from 47 wt.% to 62 wt.% Ti in order to shift the *composite* composition closer to the optimum $H_{c2}$ composition of Nb 44 wt.% Ti. A clear trend of increasing $H_{c2}$ with decreasing pin size was present in the Nb 62 wt.% Ti matrix APC composite, direct evidence of proximity-effect $H_{c2}$ enhancement. However, the extent of enhancement was significantly less than predicted in the fully coupled limit, even when the pin thickness was much smaller than $\boldsymbol{x}$. The discrepancy between predicted and observed behavior is evaluated within the context of proximity-effect models for Nb/Ti thin film multilayers.

Chapter 6 then tests the magnetic pinning model proposed by Cooley, Lee, and Larbalestier. The proximity length of pure Nb was decreased by 30% and 60% via separate alloying additions of 7.5 wt.% Ta and 10 wt.% W, respectively. The functional dependence of the bulk flux pinning force on field, $d_p$ and $\boldsymbol{x}_N$ agreed qualitatively with the magnetic pinning model.

Chapter 7 summarizes the conclusions that can be drawn from this work.

# 2. APC wire design, fabrication, and characterization

The basic premise governing APC wire fabrication is that a spatially uniform two-dimensional array of Nb-Ti and a non-superconducting pin material can be assembled at a macroscopic size, i.e. when the pins are $10^{-3}$–$10^{-2}$ m in diameter, and then reduced through a series of extrusion, drawing and re-stacking steps until the pin size and spacing are comparable to the fluxon core diameter 2$\boldsymbol{x}$ and spacing $a_0$, i.e. $10^{-8}$ m at 4.2 K and $2.2 \times 10^{-8}$ m at 5 T. No other metalworking process requires a comparably large deformation strain of order 20–25 and only because of the extreme ductility of Nb-Ti alloy can such a process be considered. The entire process is illustrated by the flow chart shown in Figure 2.1.

Figure 2.1: Fabrication flow chart for APC wires. The bar shown represents stages of the reduction sequence; the long gray segments represent extrusion steps, while the short, darker segments represent cold drawing steps. The horizontal arrows indicate where the re-stacking steps occurred. The specific flow chart shown corresponds to composites fabricated in Chapters 4–6.

At the crux of the fabrication process are several sub-element re-stacking steps which allow for simultaneous control over the pin, filament, and wire diameters. Each stage is described below in general terms, with specific details provided in chapters 3–6 where the specific composites are discussed.

## 2.1 Wire Design

The design of APC composite wires requires consideration on two size scales, the first scale being the *nanometer* length scale of flux-pinning centers, as discussed above, and the second being the *micrometer* subdivision of superconducting Nb-Ti filaments within the Cu matrix. The following sub-sections detail the designs of the pin array and the filament array.

### 2.1.1 Pinning array design

To first order, APC designs satisfy two basic criteria. Since vortices are uniformly distributed in the flux line lattice, the pinning centers should also be uniformly distributed in the superconducting matrix in order to maximize the number of vortex–pin interactions. Second, most applications require isotropic flux pinning for any field orientation perpendicular to the wire axis.

Despite the rather large number of APC designs shown in Figure 1.6, the effect of starting pin arrangement has not been systematically studied. However, no design has functioned particularly well or poorly, either. Complicating this issue is the fact that the pinning center shape and arrangement at *optimum* size seldom resemble the shape

expected from the design, as shown in the few studies where optimized nanostructures have been revealed by transmission electron microscopy [29, 39, 54]. Thus, it is still not at all clear whether the starting pin geometry is important.

Our designs therefore emphasized *uniform*, *isotropic* pin arrangements. Round pins are a good choice since their shape is well defined and the progressive degradation of their shape with drawing strain can be routinely characterized with the image analysis algorithms of Lee, Jablonski, and Larbalestier [55]. The island-type process [Figure 1.6(f)] is ideal since both the pin spacing and volume fraction are determined by the diameters of the pin and the Nb-Ti tube. The rod-based process [Figure 1.6(d)] offers less control over the pin spacing and volume fraction, but also offers the requirement of using only rods for starting components; the difficulty associated with gun-drilling a Nb-Ti tube is avoided. The composites in this thesis were assembled using both techniques. In the early stages of fabrication process development, the rod-based technique was used. Once the composite billet design and the thermomechanical parameters which control deformation during extrusion and drawing were better understood, island-type designs were chosen because of the more precise control over the pin diameter and spacing they afforded.

*2.1.2  Selection of pin material, pin fraction, and matrix composition*

Since we had little previous experience with large-strain, multiple-extrusion APC techniques, our first goal was to develop the fabrication process. To this end, Nb was selected as the pinning center material due to its high ductility, and mechanical and

chemical compatibility with Nb 47 wt.% Ti.  Since similar Nb-pin composites had been fabricated previously by others using several different fabrication techniques, one goal of our early work was to make a direct comparison of our composite to others.  This consideration also guided our initial selection of a 25% volume fraction and a Nb 47 wt.% Ti matrix composition.  Once the processing parameters were well understood, both the matrix and pin compositions were varied in subsequent composites with only slight changes made to the processing parameters.

### 2.1.3  Process design

Since a typical single-stack reduction schedule used to make conventional Nb-Ti wires allows for a total strain of 11–15 (e.g., reducing a 1.5–25 cm dia. billet to 0.1 mm dia. wire), several re-stacking steps are necessary to accumulate the requisite strain of 20–30. The number of stacking steps ($n$) required for this purpose partially depends on the desired characteristics of the final wire, specifically the nominal pin diameter ($d_p$), wire diameter ($d_w$), copper-to-superconductor ratio ($R$) and pin volume fraction ($V_p$).  These four parameters can be used to calculate the total number of pins ($n_p$):

$$n_p = (d_w/d_p)^2\, V_p\,(1+R)^{-1}. \tag{2.1}$$

$n_p$ serves as a global design parameter and is used to quantify the relationship between $n$ and the number of elements per stack ($n_e$) for each fabrication technique:

$$n_e = (n_p/V_p)^{-n} \qquad \text{rod-based} \tag{2.2a}$$

$$n_e = n_p^{-n} \qquad \text{island-type} \tag{2.2b}$$
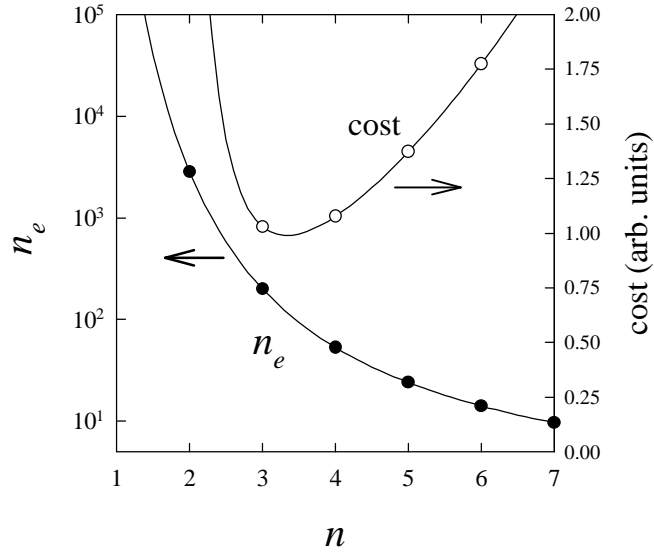
Figure 2.2: Design considerations for APC wires. The number of stacked elements ($n_e$) is plotted as a function of the number of extrusions ($n$) needed to manufacture an APC wire, using typical input parameters of $d_p$=20 nm, $d_w$=80 µm, $V_p$=0.25 and $R$=1.5. Also shown is the cost as a function of $n$, where $\text{cost} \propto n(n_e + 300)0.9^{-n}$. Note that the $n_e$ scale is logarithmic while the cost scale is linear. In practice, 3 or 4 stacking and extrusion steps were used, corresponding to minimum cost.

Using typical final wire design parameters ($d_p = 20\,\text{nm}$, $d_w = 80\,\mu\text{m}$, $V_p = 0.25$, and $R = 1.5$) the relationship between $n$ and $n_e$ is shown graphically in Figure 2.2 for a rod-based wire design. The choice of $n$ was largely determined by cost. Figure 2.2 shows the cost (in terms of total labor input to fabricate a given APC wire) as a function of $n$. Cost is defined roughly by

$$\text{cost} \propto n(n_e + 300)0.9^{-n}. \tag{2.3}$$

In practice, 3 or 4 stacking and extrusion steps were used, which corresponds to minimum cost.

It should be noted that the curves in Figure 2.2 correspond to absolute minimum values. In practice, elements were stacked into hexagonal-shaped arrays to facilitate subsequent stacking operations, thus imposing a geometrical constraint on $n_e$. The number of elements in a hexagonal array of radius $r$ elements from center to corner is given by:

$$n_e^{hex} = 3r^2 - 3r + 1 \qquad (2.4)$$

which yields allowable $n_e$ values of 7, 19, 37, 61, 91, 127,…etc.

Thus far, this analysis has neglected consideration of the Nb-Ti filament diameter. As discussed in chapter 1, in order to avoid surface pinning contributions to the bulk pinning force, the filament diameter must be significantly larger than $l$. Conversely, large-diameter filaments are more susceptible to flux jump instability [56] at currents below $I_c$. Most commercial superconducting wires have filament diameters which range from 5–100 μm, providing a good guide for APC wire design. Here, the final filament diameter range was determined by the extrusion stage at which the copper cladding was removed prior to re-stacking. Prior to that step, a 55-filament stack was made to better approximate a round filament, as shown in Figure 4.1(a).

## 2.2  Wire fabrication

### 2.2.1  Composite billet design

A hexagonal-shaped bundle of Nb-Ti and pin material rods [Figure 1.6(d)] was used to assemble rod-based APC wires, while a rod of the pin material and a Nb-Ti tube [Figure

1.6(f)] were used to assemble island-type APC wires. In both cases the outer dimension of the stack was designed to fit within a 15.6 mm O.D. copper can, this dimension fixed by the 15.9 mm inner diameter of the extrusion chamber bore, the ~0.3 mm difference used to accommodate thermal expansion of the billet during pre-heating, and the space for the hydrostatic fluid. The inner diameter of the Cu can determined the composite copper-to-superconductor ratio. Since Cu is significantly softer than Nb-Ti and the ratio of their flow stresses depends on temperature, the volume ratio of the two metals and the extrusion temperature control the uniformity of deformation during extrusion and drawing. Choice of extrusion temperature is discussed in more detail in section 2.6.

### 2.2.2  Composite billet assembly

Figure 2.3 schematically illustrates the components of a typical extrusion billet. The process and apparatus for billet fabrication by extrusion were based on methods developed previously by Jablonski [39]. Extrusion cans were made by welding an end cap onto one end of a Cu tube. The cans were welded in an argon-filled glove box using a motor-driven fixturing assembly which rotated the can circumferentially at 6 RPM beneath a stationary tungsten inert gas (TIG) welder. After end cap welding, the extrusion can was removed from the glove box. Prior to billet assembly, all Cu components were etched in a solution of 50% $HNO_3$ and 50% $H_2O$ to remove surface contamination and then ultrasonically cleaned in methanol. Nb-Ti and pin components were not etched to avoid altering their dimensions, but were instead twice cleaned in methanol.
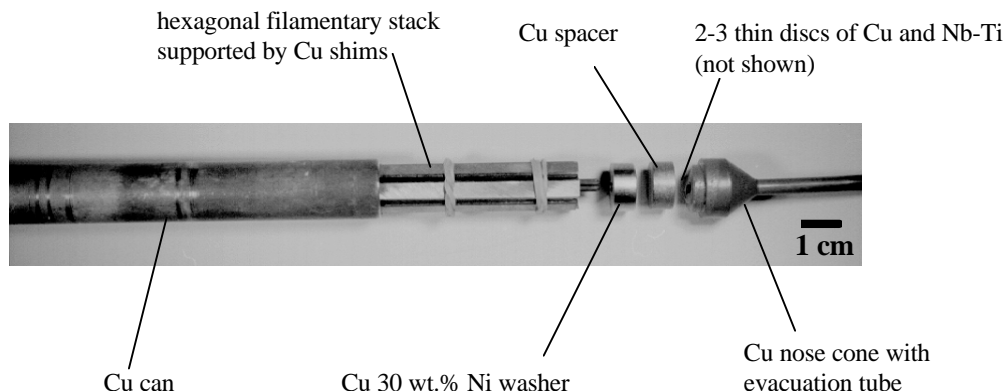
Figure 2.3:  Extrusion billet components prior to assembly.

Following rinsing and drying, billet components were transferred into the glove box for composite assembly and nose cone welding.  A nose cone was welded onto the can using the same procedure as described previously for end-caps.  After welding, fully assembled extrusion billets were evacuated to ~$10^{-2}$ Pa for ~5–10 hr with a diffusion pump and temporarily sealed by cold forging a ~50 mm length of the evacuation tube, the final seal being made by TIG welding over the seam.  Finally, the evacuation tube was swaged to ~2.5 mm diameter to allow for clearance through the extrusion die.

In order to remove much of the void space prior to extrusion, billets were compacted to 240 MPa by cold isostatic pressing (CIP).  In preparation for isostatic pressing, a billet was inserted within a 20 mm diameter, 1 mm thick rubber CIP bag, then the bag was evacuated and sealed with rubber bands.  After isostatic pressing, the outer diameter of the billet was machined to a final tolerance in preparation for extrusion.  Whenever

possible, extrusion billets were machined to a uniform outer diameter of $15.6 \pm 0.03$ mm. However, sometimes sections of the pressed billet compacted to less than 15.6 mm diameter in juxtaposition to the hexagonal-shaped filament bundle contained within. In that case, the length of the billet adjacent to the filaments was machined to a slightly smaller diameter, typically 14.5–15.0 mm, while each end was machined to 15.6 mm to allow for concentric alignment of the billet within the extrusion chamber. A compound angle ($35^o / 40^o$ half angle) was machined into the nose cone to provide a good seal with the extrusion die ($37.5^o$ half angle).

### 2.2.3  Extrusion

As discussed earlier, the large reduction strains required for APC wire fabrication generally require 2–4 element re-stacking steps. In order to facilitate strong bonding amongst the elements and minimize end losses, each re-stack is usually extruded warm ($<0.5T_m$, where $T_m \equiv$ melting temperature). Moreover, the bonding of bare Nb-Ti elements, a key requirement for maintaining a large ($>>1$) Nb-Ti filament size, is extremely difficult, if not impossible [57], without warm extrusion or elevated temperature sintering.

Uniform extrusion of bimetallic composites becomes increasingly difficult as the ratio of flow stresses becomes large, even for simple axisymmetric deformation processes such as extrusion and drawing. Analytical solutions for bimetallic composite extrusion and drawing, and analysis of common composite failure mechanisms are covered extensively by Avitzur [58, 59, 60, 61, 62]. However, many variables enter the deformation

equations, several of which are difficult to quantify. In the present work, several variables such as die angle and reduction ratio were selected according to previous guidelines provided by Jablonski [39], who utilized a compendium of data provided by Collings [63].

Homogeneous or *sound* composite flow is the principal objective of any extrusion, thus, to first order the extrusion parameters were chosen to satisfy this condition. The yield strength of face-centered cubic (fcc) metals such as Cu is rather temperature-independent to high homologous temperatures while that of body-centered (bcc) cubic metals such as Nb and Nb-Ti decreases as a result of thermally activated slip [64]. Therefore, increasing the extrusion temperature decreases both the overall flow stress and the flow stress differential between Nb-Ti and Cu and expands the processing parameter space for homogenous composite deformation. In practice, conventional Nb-Ti composites are usually extruded at 500–650 $^{\circ}$C [63].

However, elevated temperatures can adversely affect the APC structure. Secondary phase (e.g. *a*-Ti) precipitation, interdiffusion or reaction between the Nb-Ti and the pinning centers, and recrystallization of the Nb-Ti are all possible consequences of elevated temperature processing. Each serves to degrade the APC structure. In addition to these *intrinsic* effects, the formation of brittle Cu-Nb-Ti intermetallic compounds [65, 66] at the Cu–superconductor interface can lead to filament sausaging [67, 68, 69], which places an *extrinsic* limit on $J_c$. Thus, to second order, the extrusion parameters were selected to avoid or at least minimize all of these deleterious side effects.
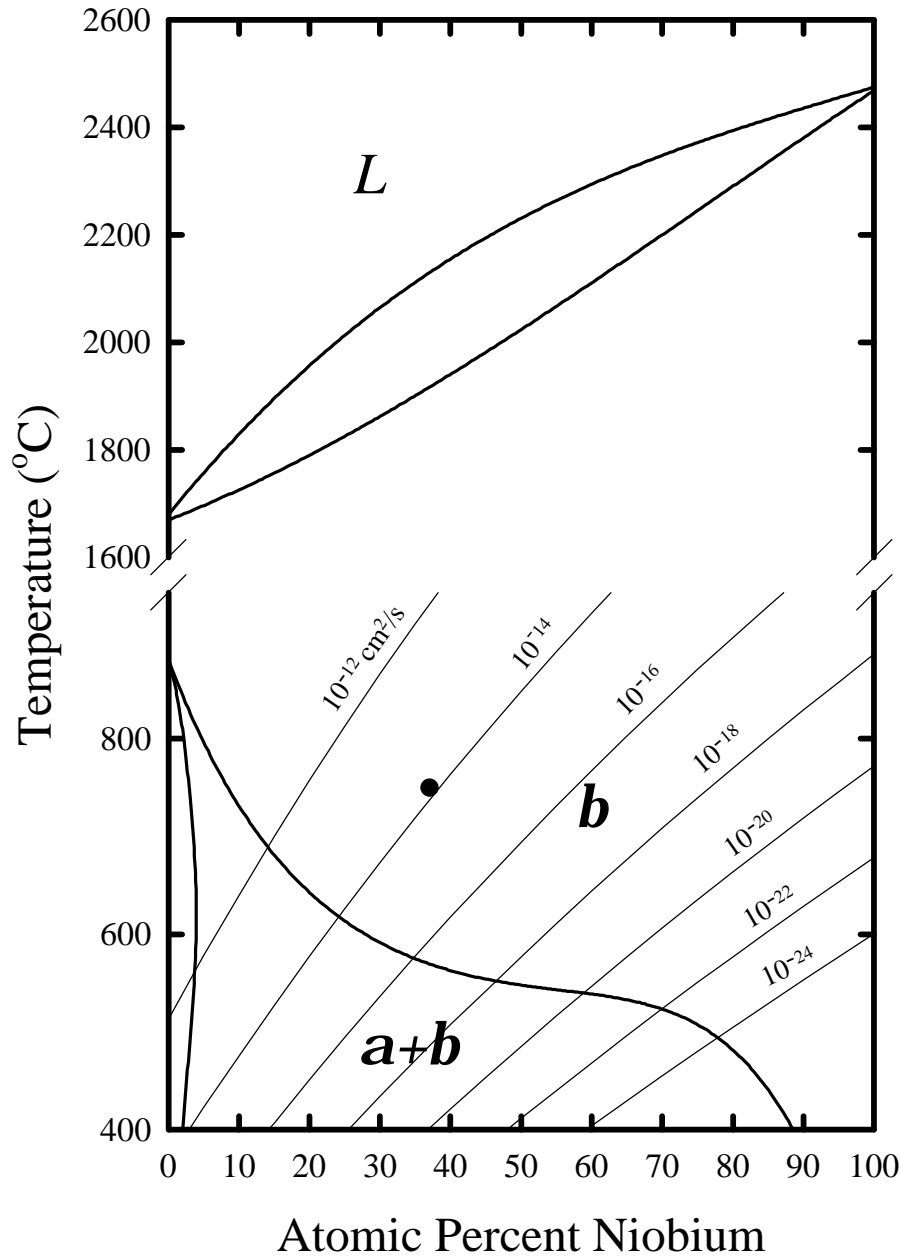
Figure 2.4:   Calculated Nb-Ti equilibrium phase diagram [70].   The thin, solid lines superimposed over the phase diagram are lines of iso-diffusivity [71].   The filled circle corresponds to the recrystallization temperature for Nb 47 wt.% Ti [72].

As the above discussion shows, the selection of an appropriate extrusion temperature requires consideration of the thermodynamics and recrystallization kinetics of the Nb-Ti system. As shown by the Nb-Ti equilibrium phase diagram [70] in Figure 2.5, the *a*–*b* transus temperature decreases with increasing Nb content. *a*-Ti can also be avoided at lower temperatures because the precipitation is kinetically limited. Both temperature boundaries depend on the Nb-Ti alloy composition and are approximately 550 and 350 $^{\circ}$C, respectively, for Nb 47 wt.% Ti. Nb-Ti interdiffusion [71] and Nb-Ti-Cu intermetallic formation [66] have a typical Arrhenius dependence on temperature, thus lower temperatures are preferred. A maximum upper limit is the Nb-Ti recrystallization temperature of 750 $^{\circ}$C for Nb 47 wt.% Ti [72]. These considerations effectively set the desirable extrusion temperature range at either below 300 $^{\circ}$C or between 550–700 $^{\circ}$C, the former interval being preferred in order to minimize interdiffusion and/or reaction. A series of initial scoping composites extruded at 250 $^{\circ}$C (corresponding to the maximum rated temperature of our extrusion chamber) broke up after 2 or 3 extrusions. Subsequently, the extrusion temperature was raised to 650 $^{\circ}$C by externally preheating the billets. This step led to the successful fabrication of our preliminary composite discussed in chapter 3.

Composite billets were extruded using a reverse hydrostatic extrusion press [73] featuring a temperature-compensated extrusion chamber [74] and a rated maximum extrusion pressure of 2 GPa. Billets were preheated for 15–20 minutes at the desired extrusion temperature. Billets extruded at 250 $^{\circ}$C were preheated in the extrusion

chamber, which was in every case preheated to 250 $^{o}$C. Billets extruded at higher temperatures were preheated in an external furnace with flowing argon and then transported quickly (10–20 s) to the chamber with a stainless steel loading tool. Billets were extruded at ~1 cm/s (billet velocity) using an area reduction ratio of 10 or 15 and a die half angle of 37.5$^{o}$. Extruded wires were immediately water quenched to avoid the precipitation of second phases.

### 2.2.4  Wire drawing and re-stacking

Prior to wire drawing, 3–6 cm was cropped from the front and back of the extruded wire. These regions comprised zones of non-uniform deformation, or "end effects". Wires were then scoured with an abrasive pad and wiped clean in order to remove the surface layer of copper oxide that was usually present following. Wires were drawn at ~5 cm/s using a 20% area reduction ratio per die pass and 11.5$^{o}$ die half angle.

Wire was drawn to the appropriate diameter for re-stacking, usually 1–1.5 mm diameter. The resulting length of wire was then divided by the number of filaments required for the next stack, plus a few extra. Seven filaments, corresponding to the center-most filaments in the stack, were cut 6.4 mm longer than the rest. These filaments protruded through a Cu 30 wt.% Ni washer (shown in Figure 2.3) at the front of the billet and served to reduce the breakthrough extrusion pressure at the front of the filamentary stack, a technique commonly used in industry for large scale billets. The Cu was then completely etched off using a mixture of 50% $HNO_3$ and 50% $H_2O$ depending

on whether the wire was to be subsequently incorporated into a monofilament or a multifilament composite. One exception to this procedure is outlined in the next section.

### 2.2.5 *Reduction of copper-to-superconductor ratio*

As a general rule, the *R* values of 1–1.5 used for homogenous deformation of extruded *monofilamentary* APC composites were also appropriate for homogenous deformation during drawing. However, the same was not true for *multifilamentary* composites, where excessive interfilamentary copper can produce uneven stress distributions in the plane transverse to the drawing direction, and ultimately lead to filament sausaging. Gregory et al. [75] associated a filament spacing-to-diameter ratio (*s/d*) of 0.12, corresponding to a local *R* value of ~0.5, with high-$J_c$ fine filamentary Nb-Ti wire. In addition, mechanical modeling of Nb-Ti composites by Guo and Warnes [76] showed that a decreasing *s/d* reduces the macroscopic stresses in the plane normal to the wire axis, thus promoting more uniform composite deformation.

In order to prevent filament sausaging in multifilamentary APC wire, we reduced the local copper-to-superconductor ratio to ~0.5 following extrusion through partial removal of the copper cladding. To remove copper in a controlled fashion, the extruded wire was immersed in a nitric acid/distilled water solution and rotated circumferentially via a motorized belt drive. This method produced excellent longitudinal and diametric variations of less than 5% and 2%, respectively, once the optimum etch concentration (30% $HNO_3$ and 70% $H_2O$) and rotation speed (10–20 RPM) were experimentally

determined. For example, the diameter of as-extruded 70 cm long wire was typically reduced from 5.1 to 3.75 mm in approximately 2 hr.

### 2.2.6  Multifilament wires

In several circumstances, 7 or 19-filament multifilament wires were fabricated by cold drawing. In preparation for stacking, the copper-to-superconductor ratio of the extruded monofilamentary wire was reduced to an appropriate value as discussed in the previous section. After etching, the wire was drawn down to 1.63 mm diameter and then drawn through a hexagonal-shaped die (1.4 mm flat-to-flat dimension) The wire was cut into 18 to 30 cm lengths for stacking inside a Cu tube (5.8 mm O.D. $\times$ 4.3 mm I.D. for a 7 filament stack and 8.2 mm O.D. $\times$ 7.1 mm I.D. for a 19 filament stack). In order to circumvent the contact of drawing lubricant with the back end of the composite, the tube was cut ~15 cm longer than the filaments and the back end was plugged with piece of modeling clay. Prior to assembly, the copper-clad filaments and tube were etched lightly in 50% $HNO_3$ and 50% $H_2O$, rinsed in methanol, and dried. Immediately afterward, the filaments were stacked, clad in Cu, and drawn through at least ten die passes; it was critical to perform these final steps quickly to obtain strong mechanical bonds between filaments, particularly when the ambient humidity was high. Wire breaks occurred infrequently during multifilament drawing, and when they did occur it was almost always a result of weak interfilamentary bonding as inferred from observing the distributed, *intra*filamentary fractures.

## 2.3  Characterization techniques

### 2.3.1  Transport $J_c$ measurements

Transport critical current measurements followed standard methods established in our lab over the past decade.  Sixty cm long wire samples were wound around and soldered to a sample holder.  The sample holder consisted of a 34.9 mm diameter, 0.8 mm wall thickness stainless steel tube with thick copper rings soldered to each end.  This design provided secure sample mounting, good current transfer from the leads to the sample, and a low resistance parallel shunt for the transport current in order to prevent sample burnout above $I_c$.  A helical groove with a twist pitch of 3.15 turns per centimeter positioned the samples on the stainless steel tube.

The applied field for transport $J_c$ measurements was supplied by either a 12 or a 14 T (4.2 K) superconducting solenoid manufactured by Oxford Instruments.  Four voltage taps were soldered to the sample at 11 cm intervals that corresponded to successive turns around the helical sample.  The maximum tap spacing of 33 cm was used for most measurements of the voltage ($V$).  The transport current ($I$) was determined by measuring the voltage across a calibrated shunt resistor connected in series to the power supply.  A computer-controlled interface was used to ramp the transport current and acquire the $V(I)$ data from two digital voltmeters connected to computer via a GPIB interface.  $V(I)$ curves were fitted with the power law expression, $V \propto I^n$, in the superconducting-to-normal transition region.  $J_{ct}$ was determined by the intersection of the fitted data with a $10^{-14}$ $\Omega$-m resistivity criterion, using the superconductor cross-

sectional area as the characteristic cross-section for determining the resistivity criterion.

Wire diameters were measured to a precision of 0.0005 mm using a calibrated

micrometer.

Copper-to-superconductor area ratios were determined by weighing a length of wire,

etching the Cu off using a mixture of 50% $HNO_3$ and 50% $H_2O$, and weighing the

superconductor.  $R$ was calculated by:

$$R = (m_{Cu}/m_c)(D_c/D_{Cu}) \qquad\qquad (2.5)$$

where  $m_{Cu}$,  $m_c$  and  $D_{Cu}$,  $D_c$  are the masses and densities of copper and the

superconductor (Nb-Ti matrix plus pin), respectively.  Mass measurements were made

using an electronic balance with an sensitivity of 0.1 mg.  Samples typically weighed 0.5

g.  A density of 8.95 g/cm$^3$ was used for copper, while the superconductor density was

calculated using the composite volume-fraction rule [64]:

$$D_c = D_p V_p + D_m (1 - V_p), \qquad\qquad (2.6)$$

where $D_p$ and $D_m$ are the densities of the pin and the Nb-Ti alloy matrix, respectively.

*2.3.2  Magnetization measurements*

Magnetization measurements were used to determine $H_{c2}$ and the irreversibility field

($H^*$).  In addition, $J_c$ can be determined indirectly through application of an appropriate

critical state model to the irreversible magnetization hysteresis ($\Delta M$).  This method for

determining the magnetization critical current density ($J_{cm}$) is particularly attractive since,

unlike $J_{ct}$, it can be measured continuously with field.  For the present work, a vibrating

sample magnetometer (VSM) was used to measure $M(H)$ loops at temperatures from

2.2–10 K and fields from 0 to $H_{c2}(T)$. The reversible magnetization data at fields near and above the field of loop closure (i.e. $\mathbf{D}M=0$) were used to determine $H^*$ and $H_{c2}$, while the irreversible magnetization was used to extract $J_{cm}$ at 4.2 K and at reduced temperature. The VSM system in our laboratory was designed and constructed by McKinnell [77] and consists of a Princeton Applied Research Model 155 VSM vibrator head assembly and supporting electronics custom fit to an Oxford 14 T superconducting magnet and variable temperature insert. A detailed description of this system is given in reference [77].

Magnetization critical current density was derived from the irreversible magnetization hysteresis $\mathbf{D}M(H)$ using the Bean critical state model for a superconducting cylinder in perpendicular field [78]:

$$J_{cm}(H,T) = 3\pi\Delta M(H,T)\big/4d_f \tag{2.7}$$

$J_{cm}$ measurements made on conventionally processed Nb 44-58 wt.% Ti wires [77] and sub-micron filament diameter APC wires with Nb pinning centers [29] have shown good agreement with $J_{ct}$ measurements made on the same samples. However, in this study, we found that some wires exhibited a large discrepancy between the shape of $J_{ct}(H)$ and $J_{cm}(H)$. A study of PMAPC wires [79] showed a similar discrepancy. For the present wires, analysis of the dependence of $M(H)$ on sample length showed this difference could be attributed to the highly anisotropic critical current densities that flow parallel and perpendicular to the pinning centers. An experimental and theoretical analysis of this effect, showing the role that the anisotropic pinning nanostructure plays in determining

the longitudinal and transverse critical current densities of optimized Nb-Ti wire, is presented in Refs. [80, 81].

# 3. Properties of Nb-Ti wires with Nb artificial pinning centers

This chapter describes the development of the microstructure and superconducting properties of our preliminary Nb 47 wt % Ti composite wire containing 24 vol. % of Nb pinning centers. This combination was chosen because of its similarity to composites fabricated in other studies using different methods, thus allowing for more direct comparisons of properties. One goal has been to make a thorough nanostructural characterization so that the pinning center size and shape at optimum wire sizes are known and not just assumed. Such characterizations are seldom performed at optimum size. A second goal of this study was to measure the $J_c$, $F_p$ and $H_{c2}$ at reduced temperatures, not just at 4.2 K, so that the properties of conventional and APC wires could be compared at constant $H_{c2}$. To perform the reduced temperature study we relied primarily on magnetization measurements. During the course of taking data, the

hysteretic magnetization was found to be strongly dependent on the sample length. An experimental and theoretical analysis of this effect, showing the role that the anisotropic pinning nanostructure has on the longitudinal and transverse critical current densities of optimized Nb-Ti wires, is presented in Refs. [80, 81]. This effect is taken into account here.

## 3.1 Experimental Design

An APC composite containing a matrix of Nb 47 wt % Ti and 24 vol % of round Nb pins was fabricated using the rod bundling process discussed in chapter 2. Thirty-one 1-mm diameter Nb rods were arranged in a hexagonal array within a bundle of 96 Nb 47 wt. % Ti rods such that the center-to-center pin spacing was $1.53d_p$. This 127-rod stack was canned in Cu, and extruded at 650 $^o$C using an area reduction ratio of 15. The extruded wire was drawn to 1 mm diameter, cut lengthwise into 127 pieces and the Cu was dissolved away in a 1:1 mixture of $HNO_3$ and $H_2O$. The hexagonal-shaped Nb-Ti/Nb filaments were re-stacked, canned in Cu and a second extrusion was made under the same conditions. After a third draw, re-stack, and extrusion sequence the monofilament wire contained $\sim 5 \times 10^5$ Nb pinning centers. A part of this wire was drawn to 0.08 mm diameter, while the rest was cut into seven pieces and extruded for a fourth time. The fourth extrusion wire was then drawn to 0.08 mm diameter. Table 3.1 gives fabrication details for each composite.

Table 3.1: APC composite design and fabrication details.

| Matrix composition (wt.% Ti) | APC composition | $V_p$ | $D_c$ (g/cm$^3$) | $n_p/n_{e1}$ | $n_{e2}$ | $n_{e3}$ | $n_{e4}$ | $R$ |
|---|---|---|---|---|---|---|---|---|
| 47 | Nb | 0.244 | 6.63 | 31/127 | 127 | 127[a] | | 0.86 |
| 47 | Nb | 0.244 | 6.63 | 31/127 | 127 | 127 | 7[a] | 1.43 |
| $T_e$ (°C) → | | | | 650 | 650 | 650 | 650 | |

[a] extruded, monofilamentary composite.

Magnetic moments were measured on wire samples using the vibrating sample magnetometer. Long wire samples, ranging from 56 mm in length for the 0.360 mm diameter wire to 300 mm for the 0.080 mm diameter wire, were wound into 3 mm diameter, 1 mm long open-circuit coils. Long wire samples were used for two reasons: Longer samples provide a larger sample moment, giving higher signal resolution. More importantly, it has been demonstrated for this same set of samples, that the magnetization of APC wires can be a very strong function of the wire length-to-diameter ratio [80]. Long lengths give better agreement between the $J_{ct}$ and the magnetization critical current density $J_{cm}$. The sample-length dependence comes from the fact that the magnetization-induced current must cross the filament in a direction perpendicular to the wire axis towards the ends of each filament and because the anisotropic pinning nanostructure of the wires produces a $J_c$ perpendicular to the axis of the pinning centers which is up to ~100 times less than that flowing parallel to the pinning centers along the wire axis. To obviate these concerns, moment measurements were made with the applied field parallel to the coil axis on long samples, so that the field was perpendicular to the long wire axis and currents were induced to flow along the whole wire length. A field sweep rate of 0.05 T/s was used, except near $H_{c2}$, where it was reduced to 0.02 T/s to increase the field resolution in the region of magnetization loop closure. The magnitude of the hysteretic moment depended only weakly on the field sweep rate for these APC monofilament samples. Magnetization critical current densities were derived from the hysteretic magnetization of the long samples using the Bean model for a
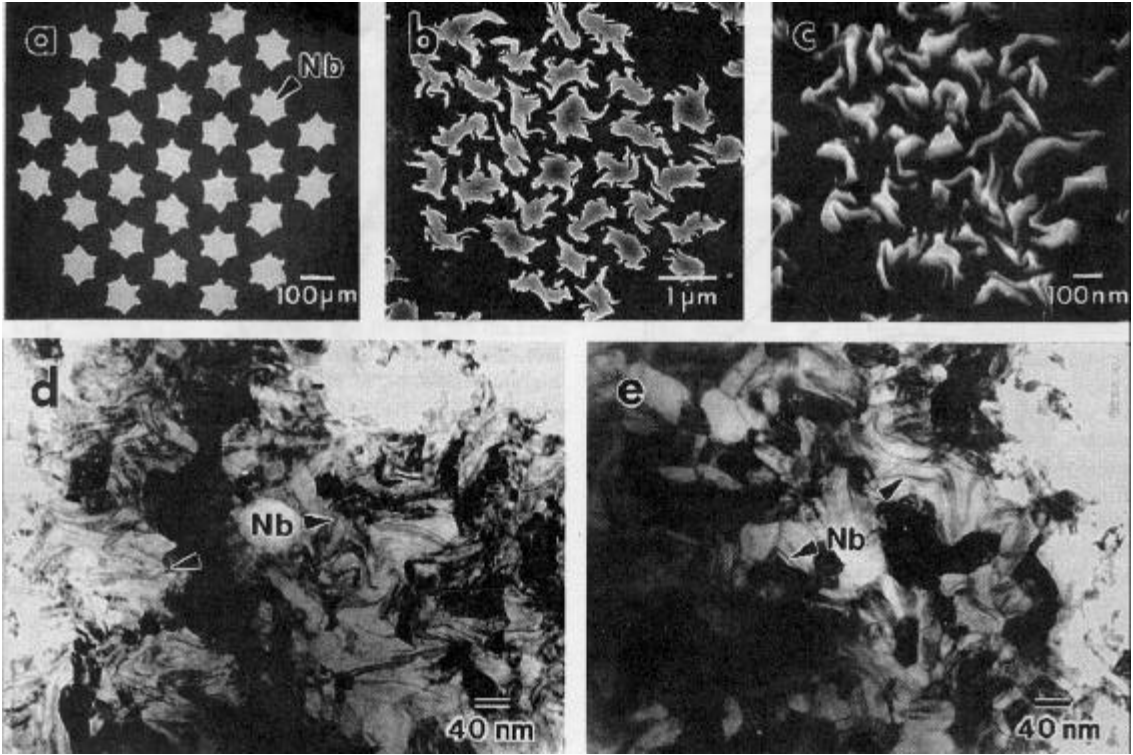
Figure 3.1: SEM micrographs of the Nb pinning center array at (a) $d_p$=100 μm, (b) 600 nm and (c) 100 nm and TEM micrographs at $d_p$=40 nm for the third (d) and fourth (e) extrusion composites. The micrographs show the development of the round pinning centers into highly aspected ribbons. At $d_p$=40 nm the actual measured pin thickness ranged from 1–16 nm for both the third and fourth extrusion composites (TEM photos courtesy of Dr. P.J. Lee).

cylindrical superconductor in perpendicular field (Equation 2.7). Magnetization runs were made at temperatures from 3–10 K in fields up to 12 T. Transverse wire cross-sections were analyzed by Scanning (SEM), Field Emission Scanning (FESEM) and Transmission Electron Microscopy (TEM).

## 3.2 Results

Figure 3.1 shows progressive deformation of the nominally round Nb pinning centers during reduction of the nominal pin diameter. The calculated nominal pin diameter is commonly used to describe the pinning center dimension, it is given by:

$$d_p = d_w / (N_p / V_p (1+R))$$ (3.1)

Following the first extrusion, at $d_p$=100 μm [Figure 3.1(a)], the pins had a hexagonal shape with an irregular surface. The six-fold star shape arises from the deformation of the round rods during the extrusion. After the fourth extrusion, at $d_p$=600 nm [Figure 3.1(b)], the pin shape became more irregular, with fine tendrils extending from the pin surfaces. The hexagonal pin geometry, though degraded, is still apparent. At $d_p$=100 nm [Figure 3.1(c)], the pins had deformed into ribbons with aspect ratios of 3:1–10:1. Figures 3.1(d) and 3.1(e) show TEM images of the pins at $d_p$=40 nm for the third and fourth extrusion composites, respectively. The microstructural contrast in the TEM images comes principally from two sources. One is Bragg diffraction from suitably oriented Nb-Ti grains, these appear as the approximately equiaxed features seen prominently in Figure 3.1(e). The residual contrast is dominated by the local atomic number. Nb ribbons are thus darker than the Nb-Ti matrix and are visible within the Nb-Ti grains. The Nb ribbons of both wires exhibit large aspect ratios. The measured pin thickness varies from <1 to 16 nm. In neither of these pictures is the original hexagonal arrangement of the pins apparent. At $d_p$=15 nm, some 1 nm thick pins could be observed in TEM images, but the pins were very difficult to discern at this stage.
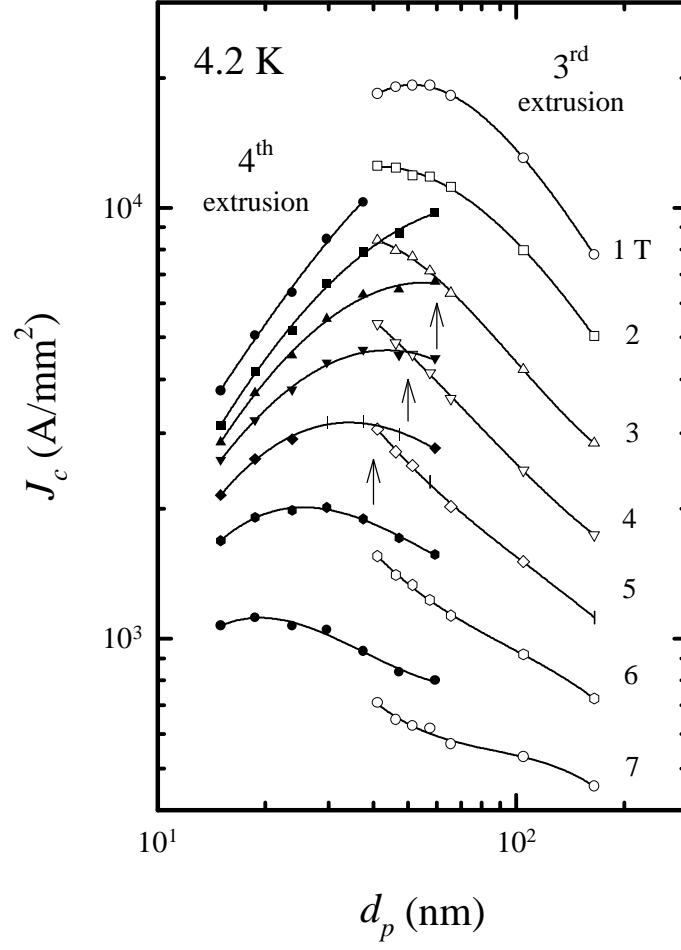
Figure 3.2: $J_c$ as a function of $d_p$ for applied fields from 1 to 7 T at 4.2 K. The curve sets from 165–40 and 60–15 nm correspond to the third and fourth extrusion composites, respectively. The vertical arrows indicate overlap points between the two curve sets.

Figure 3.2 shows the transport critical current density as a function of $d_p$ for applied

fields ranging from 1–7 T. Two sets of data are shown: that for the third extrusion

covers the range of $d_p$ from 165 to 40 nm and that for the fourth ranges from 60 to 15 nm. $J_c$ increases at all fields except 1 T with decreasing $d_p$ for the third extrusion composite. At 1 T, the peak $J_c$ was 20 kA/mm$^2$ for $d_p$=50 nm, while at 5 T, it was 3.2 kA/mm$^2$ for $d_p$=35 nm. In the pin diameter interval where the third and fourth extrusion $d_p$ values overlap, $d_p$=40–60 nm, there is poor agreement between the data. There is also a crossover in $J_c(d_p)$ as the field is increased. From 1–3 T the third extrusion composite $J_c$ values exceed those of the fourth. From 3–5 T, crossover points are indicated by the vertical arrows in Figure 3.2 and from 5–7 T, the fourth extrusion $J_c$ values exceed those of the third. The fourth extrusion composite exhibits $J_c$ peaks at progressively smaller $d_p$ values as the field is increased, where peaks of 40, 35, 25 and 17 nm occur for fields of 4, 5, 6, and 7 T, respectively. As is clear from Figure 3.1, the actual pin thickness is, in all cases, much smaller than $d_p$.

Figure 3.3 shows the bulk flux pinning force curves of the APC composite at 4.2 K as $d_p$ is reduced from 165 to 15 nm. The large arrows follow the maximum in $F_p$ as the pin size is reduced. For $d_p$=165 nm, the largest pin diameter wire measured, $F_p(H)$ decreased almost linearly with increasing field. As the pin size was reduced, a low field maximum in $F_p(H)$ emerged. The maximum value $F_p$ of 25 GN/m$^3$ occurred at 2.5 T for $d_p$=40 nm. As the pin size was reduced further, the peak in $F_p(H)$ shifted to higher fields and the shape of $F_p(H)$ tended towards that of conventionally processed Nb 47 wt.% Ti, but the peak magnitude declined rapidly, as seen for $d_p$=15 nm.
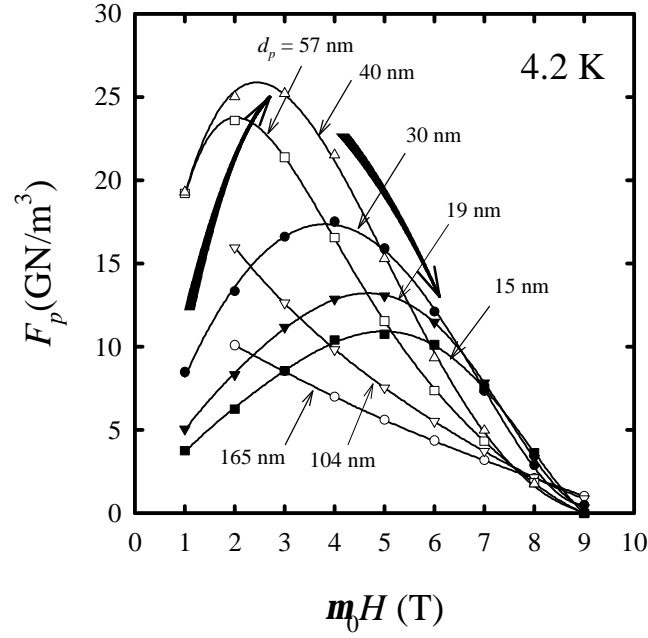
Figure 3.3: $F_p(H)$ as a function of $d_p$ as derived from the transport critical current measurements at 4.2 K. The filled and open symbols correspond to third and fourth extrusion composites, respectively. The long arrows follow the maximum in $F_p(H)$ as the pin size $d_p$ is reduced.

Figure 3.4 shows the magnetization $M(H)$ near $H_{c2}$ for $d_p$=165, 40 and 15 nm at 4.2 K. In addition to the hysteretic magnetization caused by flux pinning, there was a small ($c$~$2\times10^{-4}$) paramagnetic moment contribution from the Nb-Ti. This contribution, together with a small signal from the Pyrex sample rod, were identified by making measurements at 10 K, above the critical temperature $T_c$ of 9.2 K for Nb 47 wt.% Ti. Both contributions were subtracted from the data of Figure 3.5. These data show that the hysteresis loop appears to close not at $M$=0 but at $M$<0. We initially identified this closure field as the irreversibility field $H^*$, thus following similar conventions used by
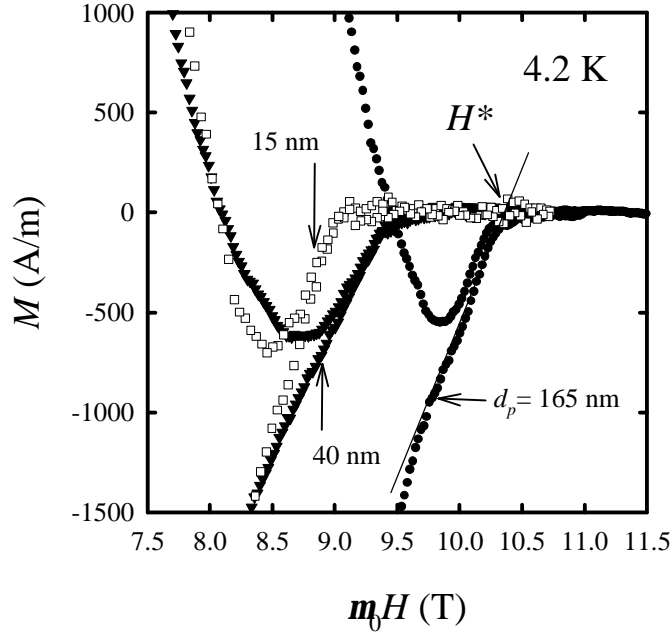
Figure 3.4: *M* as a function of $m_0H$ near $H_{c2}$ for $d_p$=165, 40 and 15 nm. The irreversibility field $H^*$ is the field at which the negative arm intersects $M$=0. $H_{c2}$ occurs at a slightly higher field and cannot be discerned from the data shown. A residual paramagnetic moment was subtracted from each magnetization curve.

Suenaga et al. [82] for conventional Nb-Ti and Bonney, Willis, and Larbalestier [83] for SnMo$_6$S$_8$. However, during subsequent magnetization measurements discussed in more detail in chapter 5, it was discovered that the downturn in $\Delta M$ near $H_{c2}$ was, in fact, an artifact caused by a small offset from center in the sample position between the VSM search coils. In fact, $H^*$ is the field at which a linear extrapolation of the lower branch intersects $M$=0. The $H_{c2}$ transition occurs at even higher fields and could not be discerned from these data due to inadequate moment signal sensitivity. However chapter 5 discusses subsequent corrections made to the measurement procedure which allowed for the detection of both $H^*$ and $H_{c2}$ on advanced composite designs.

Table 3.2: Irreversibility field as a function temperature for the APC wires at $d_p$=165, 40, and 15 nm and for an optimized, conventionally processed Nb 47 wt.% Ti wire at 4.2 K.

| $d_p$ (nm) | $m_0 H^*$ (T) | | |
|---|---|---|---|
| | 4.2 K | 3.5 K | 3 K |
| 165 | 10.3 | … | … |
| 40 | 9.5 | 10.7 | … |
| 15 | 9.0 | 9.8 | 11.0 |
| conventional Nb 47 wt.% Ti | 10.7 | … | … |

Table 3.2 lists the measured $H^*$(4.2 K) values as a function of nominal pin diameter and temperature. $m_0 H^*$ decreased from 10.3 to 9.5 to 9 T in going from $d_p$=165 to 40 to 15 nm. For comparison, $m_0$H* for an optimized, conventionally processed wire at 4.2 K is 10.7 T [84], a value of 1.2 T higher than the highest flux pinning ($d_p$=40 nm) APC sample. This strong suppression of $H^*$ in the APC composite complicates direct comparison of APC and conventional wire properties.

## 3.3 Discussion

### 3.3.1 Microstructure

In this study, as in the few other studies which have explicitly observed the microstructure at optimum wire size, it is abundantly clear that the real pin thickness is considerably smaller than the round wire approximation, $d_p$. The ribbon-like shape developed by the Nb pinning centers is a general consequence of the <110> drawing texture which develops in body centered cubic (bcc) metals subjected to the axially

symmetric deformation of wire drawing [85, 86, 87]. In the early stages of drawing, individual grains rotate, such that a <110> direction is aligned with the drawing axis. Slip is then restricted to the two <111> directions which lie within the {110} plane containing the <110> texture. The resultant plane strain deformation, combined with the requirement of grain boundary continuity, forces the grains to intercurl, slowly transforming into ribbons. In the case of the conventionally produced *a*+*b* two-phase microstructure, the bcc *b*-Nb-Ti grain texture development causes the hexagonal close packed *a*-Ti precipitates to transform into ribbons. In the APC composite, both Nb and Nb-Ti are bcc, so it is likely that both pin and matrix contribute to the ribboning, as is the case for Nb diffusion barriers in conventionally processed Nb-Ti wire [88, 89].

It is worth noting that the pin shape seen here, at least in the later stages of development, parallels that seen in an earlier study by Cooley et al. of a somewhat similar APC composite. In that case the pins of Nb 1 wt.% Ti were inserted into gun-barrel-drilled holes and, aside from the initial warm extrusion of the original 150 mm diameter Nb 47 wt.% Ti / Nb 1 wt.% Ti, all subsequent composite fabrication was done by cold drawing. The shape of nominal 600 and 100 nm diameter pins of the present composite are comparable to the shape of the 200 and 32 nm diameter pins of the earlier study. The difference in the onset of pin shape degradation is likely due to differences in processing methods, for in the present case, the pins were given an anneal at ~1 mm diameter just prior to the stacking of the billet and three or four warm (650 $^{o}$C) extrusion steps were then used during wire reduction, thereby increasing the tendency for

polygonization or recovery of the Nb-Ti grains, either of which would increase the ratio of the Nb-Ti grain size to Nb-pin diameter and cause more rapid pin shape degradation. Thus the use of the nominal pin diameter as a quantitative tool can be somewhat misleading, since two APC composites of not greatly dissimilar design can have significantly different pinning microstructures for the same value of $d_p$. However, the use of $d_p$ is so widespread in the literature and there is so little quantitative microscopy near optimum sizes that it is still useful to report properties as a function of $d_p$. Quantitative understanding of the dependence of properties on microstructure clearly requires observation of the microstructure.

The maximum $F_p$ for the APC composite occurs for $d_p$=40 nm where the actual measured pin thickness is quite variable, ranging from <1 to 16 nm as shown in Figures 3.1(d)–(e). This large pin thickness range contrasts strongly with the thinner, more uniform pins observed in optimized, conventionally processed Nb 47 wt.% Ti, where the *a*-Ti ribbon thickness ranges from 1 to 5 nm. Although there has been little explicit study of the role that the distribution in pin thickness plays, a wide distribution is almost certainly detrimental to $J_c$, as emphasized in recent studies of powder metallurgy APC composites [39, 55] and also in inhomogeneous conventionally processed Nb-Ti [].

*3.3.2  $J_c$ vs. $d_p$*

The $J_c(d_p)$ curves of Figure 3.2 clearly illustrate that the optimum pin size is a function of magnetic field, the peak $J_c$ moving towards smaller pin sizes as the field is increased. This agrees qualitatively with the results of Matsumoto et al. [33] with the exception

that, at a given field, their pins optimized at approximately half the nominal pin dimension that is reported here.  This difference may reflect the fact that their composite was made from a planar pin array, which yields a smaller pin *density* than round pin arrays for a fixed nominal pin dimension $d_p$.  Justification for this hypothesis is provided in chapter 4.

The difference in $J_c$ behavior between the third and fourth extrusion composites of the present study must be related to a difference in their flux pinning microstructures.  However, a comparison of the microstructures at $d_p$=40 nm, shown in Figures 3.1(d) and 3.1(e), does not reveal any obvious differences between the average pin thickness or pin thickness distribution, for in both cases, the measured pin thickness varied from ~1–16 nm.  A plausible explanation for the difference is that the fourth extrusion (carried out at 650 $^{o}$C) caused additional pin/matrix interdiffusion.  This could change the pinning microstructure in several ways, one way being that diffusion would tend to degrade the pin/matrix interface, thus diminishing the strength of the pinning wells.  This appears to be the case at low fields where the $J_c$ of the fourth extrusion composite is lower than that of the third.  However, this is not the case at higher fields, where an enhancement of the fourth extrusion composite $J_c$ is observed.  Another consequence of interdiffusion which could explain this high-field $J_c$ enhancement is that the interdiffusion would serve to alloy the pins, thereby reducing their normal state coherence length, and causing the elementary pinning force to optimize for thinner pins.  Assuming, as usual, that full summation of the elementary pinning forces occurs, this would lead to a relative

enhancement of the high field $J_c$, just as is observed. Unfortunately, the sub-micron pin diameter directly following the fourth extrusion prevented a quantitative analysis of pin/matrix interdiffusion to made.

### 3.3.3  $F_p(H)$ curve shapes

Figures 3.1–3.4 present a clear picture of the microstructure and superconducting properties of this Nb pin APC composite as the pin size is reduced. The largest bulk pinning force occurred for pins whose measured average thickness was ~8 nm, a value which is considerably thicker than the 1–5 nm thick *a*-Ti ribbons found in optimized conventional Nb-Ti. The greater optimum thickness of the Nb-pin APC composite is in accordance with the magnetic pinning model, which predicts that the pin thickness at which $F_p$ is maximum is ~$x_N$/3, where $x_N$ is the pin proximity length. Measurements [90] show that the $x_N$ of Ti is ~3 times shorter than that of Nb; the $x_N$ of *a*-Ti is undoubtedly even shorter because it alloyed with ~5 at.% Nb [22].

The magnetic pinning model can also be used to describe the changes in $F_p(H)$ with decreasing pin size that occur in the present composite. At peak $F_p$ ($d_p$=40 nm), the elementary pinning force $f_p$ is slightly less than its maximum value and the pin thickness is approximately equal to $x_N$/3. Since $x_N$/3 is rather large for Nb pins (~27 nm) the pin number density corresponding to pins of this thickness is low and this also corresponds to a fluxon density characteristic of low fields. As the pin size is reduced further, the pin density increases. However, the strong decrease in $f_p$ which occurs for thinner pins cannot be properly compensated by the increase in pin-vortex interaction density. The

net result is that $H_{max}$ increases but the magnitude of $F_{pmax}$ decreases, as is clearly shown in Figure 3.3.

*3.3.4  H\* vs. $d_p$*

That the irreversibility field declines as $d_p$ is reduced is clear from Figure 3.4.  As $d_p$ is reduced from 165 to 15 nm, $m_0H^*$(4.2 K) declines from 10.3 to 9 T.  This reduction is consistent with proximity-effect mixing of the matrix and pins at the final size.  The overall composition of 76 vol.% of Nb 47 wt.% Ti matrix and 24 vol.% Nb pins is Nb 32 wt.% Ti, for which the homogenous alloy mixture $m_0H_{c2}$ is ~10.5 T as measured by magnetization [100].  This agrees with the measured $m_0H^*$ of 9 T in the APC wire at $d_p$=15 nm and is consistent with the conclusion that the pinning centers are fully coupled to the matrix.

Although the upper critical field is the critical field most often quoted for a superconductor, it is the irreversibility field $H^*$ which is of real technological importance, because $H^*$ defines the practical upper limit to $J_c$.  Fortunately, in the case of optimized, conventional Nb 47 wt.% Ti, the ~0.5 T (4.2 K) difference between $H_{c2}$ and $H^*$ is rather small, whereas in high temperature superconductors, it can be very large.  Unfortunately the quantity $H_{c2}$–$H^*$ could not be determined in this study because $H_{c2}$ could not be discerned from the $M(H)$ curves of Figure 3.4.  However, $H^*$ *and* $H_{c2}$ were determined for a series of advanced composites discussed in chapter 5.

*3.3.5  An effective comparison procedure for conventional and APC wires*

Although the proximity-effect depression of $H^*$ and $H_{c2}$ in existing APC composite designs like the present severely limits the high-field $J_c$, it is important to note that it should not pose any fundamental obstacle to developing high $J_c$ in APC conductors. Figure 3.5 shows the $F_p$ curves for the APC composite at $d_p$=40 nm (at which the highest $F_p$ was achieved) and at $d_p$=15 nm (at which the highest $F_p$ was achieved at >6 T), together with a curve for a high-$J_c$ conventionally processed Nb-Ti wire.  Extrapolating the high field $F_p$ of each curve to zero illustrates the pronounced differences in their high field behavior.  Table 3.2 shows that the measured $H^*$ of the conventional wire is between 1.2 and 1.7 T higher than the APC wires at $d_p$=40 and 15 nm.  These differences were removed by lowering the measuring temperature of the APC wires, so that the $m_0H^*$ values of the APC wires were equalized to approximately 10.7 T.  Table 3.2 shows that, at 3.5 K, the $m_0H^*$ of the $d_p$=40 nm wire is 10.7 T and, at 3 K, the $m_0H^*$ of the $d_p$=15 nm wire is 11 T.  The percentage increase in $DM$ in going from 4.2 to 3.5 to 3 K was then applied to the 4.2 K transport $F_p$ curves so as to construct the $H^*$ equalized $F_p$ curves shown in Figure 3.5.  These equalized $F_p$ curves clearly show that the Nb-pin APC composite is superior to the conventional wire at all fields up to ~7 T.  When $H^*$ was equalized, the APC composite achieved a $J_c$(5 T) of 4600 A/mm$^2$ a value which would be the highest $J_c$(5 T) ever reported in round wire Nb-Ti.  Thus it is quite clear that APC wires offer great promise for further raising the attainable $J_c$ of Nb-Ti, particularly if the overall composition of matrix and pin can be better balanced so as to
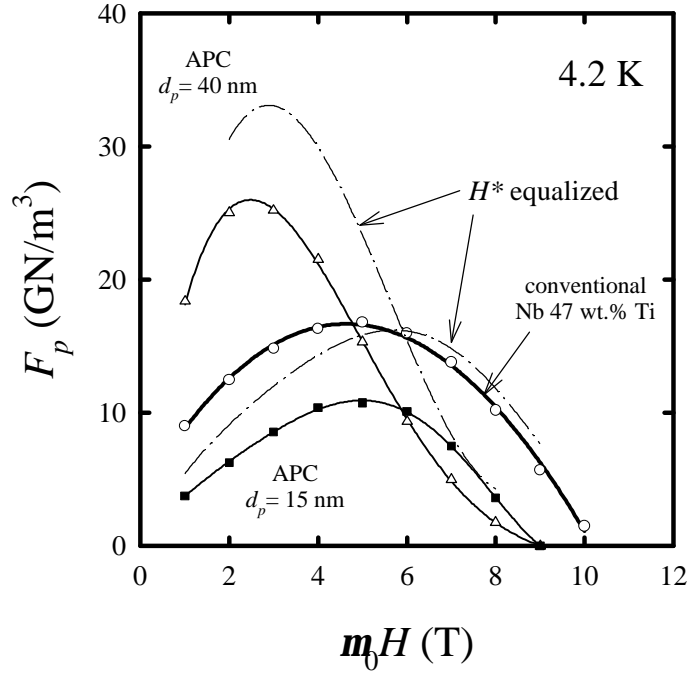
Figure 3.5: $F_p$ as a function of $m_0H$ for $d_p$=40 and 15 nm at 4.2 K (solid lines) and at reduced temperatures (dashed lines) for which the $H^*$ values are approximately equal to the values for conventionally processed Nb 47 wt.% Ti at 4.2 K. An optimized, conventional Nb 47 wt.% Ti $F_p$ curve (thick, solid line) is shown for comparison.

produce an overall Nb-Ti composition lying within the high $H_{c2}$ range of Nb 42–48 wt.% Ti. Such a composites provide the basis for chapter 5.

The fact that the $H^*$ equalized APC composite performs only marginally better than the conventional wire at high fields further supports the assertion of Cooley et al. [52] that the pin proximity length is the defining parameter for determining the field at which $F_{pmax}$ will occur. As the authors suggested there, a key to increasing the high field $J_c$ of Nb-Ti may be in decreasing the pin proximity length. APC composites designed to

improve the high field pinning through decreases in the pin proximity length are the basis

for chapter 6.

## 3.4  Conclusions

The microstructure and superconducting properties $J_c$, $F_p$, and $H^*$ have been studied for

an APC composite consisting of Nb 47 wt.% Ti with 24 vol.% of Nb pinning centers.  A

maximum bulk flux pinning force of 25 GN/m$^3$ occurred at ~$0.25H_{c2}$ when the nominal

pin diameter was 40 nm.  However, the actual pinning center thickness at this size

ranged from <1 to 16 nm.  As the pin size was further reduced, the $F_p$ peak position

shifted to higher fields, and the peak magnitude decreased.  Over this entire range of

($d_p$=165–15 nm) the irreversibility field decreased from 10.3 to 9 T.  All of these trends

are qualitatively consistent with Nb-pin APC composites of similar compositions,

fabricated by other groups using different methods.

By reducing the temperature at which the APC wires were measured, the values of

$H^*$ were equalized to the value of 10.3 T for optimized, conventional Nb 47 wt.% Ti in

order to compensate for the non-optimal composition of the matrix and pin mixture.  At

fields up to 7 T, the APC composite clearly outperformed the conventional wire,

achieving a $J_c$(5 T) of 4600 A/mm$^2$ when $H^*$ was equalized.

The $J_c$ properties of these initial APC composites compare favorably to other Nb-pin

composites of similar design by Matsumoto et al. [31], Motowidlo et al. [27], and

Cooley [29], thus demonstrating our rod-based process to be a viable method for

fabricating APC wires.  However, a significant difference in $J_c$($d_p$, $H$) behavior between

composites which received three or four warm extrusions suggests that the fourth extrusion produced a marked effect on the flux pinning nanostructure, most likely by diminishing the strength of the pinning wells through pin/matrix interdiffusion. This issue is further addressed in the next chapter.

# 4. Improved thermomechanical processing

While the thermomechanical processing steps [20, 21] and the resulting flux pinning nanostructures [21, 22, 23] of high-$J_c$ conventional Nb-Ti wire are firmly established, the same is not true for APC wires. Consequently, it is not surprising that a significant range in $J_c(H)$ is found for APC composites of nominally the same composition but manufactured via different processing routes. For instance, two groups have manufactured and characterized APC composites of similar content to the composite described in chapter 3, namely, Nb 47 wt.% Ti with 24–25 vol.% of nominally round [91] or planar [33] Nb pins. These composites produced maximum $J_c(5 \text{ T})$ values of 3200, 2400 and 2800 A/mm$^2$, respectively. Although hard evidence is lacking, it seems likely that the range in $J_c$ originates from differences in the flux pinning nanostructures. As recent work by Jablonski, Lee, and Larbalestier [39] has shown, the detailed

nanostructure of the pins exerts an important effect on the attainable $J_c$, independent of the volume fraction of pin and its composition.

A very important difference between conventional and APC Nb-Ti lies in the evolution of the flux pinning nanostructures during processing. Conventionally processed Nb-Ti alloy becomes two phase late in its processing and only room-temperature wire drawing is necessary to reduce the *a*-Ti precipitate down to optimum flux pinning thickness (1–2 nm). APC wires, on the other hand, are two-phase throughout their fabrication and some elevated temperature processing is generally unavoidable. All practical APC composites require 1–4 warm extrusion steps, usually $^\circ$C. Interdiffusion associated with elevated temperature processing can mix the pin and matrix materials, weakening the sharpness of the designed two-phase nanostructure.

Our previous study [54] described in chapter 3 and a study by Kanithi et al. [92] showed that the ultimate $J_c(H)$ behavior of APC wires containing Nb 47 wt.% Ti with Nb pins was very sensitive to the number of warm (~600 $^\circ$C) extrusions used in their fabrication. In our study, for the same nominal pin diameter, a wire which had received three 650 $^\circ$C extrusions exhibited dramatically different $J_c(H)$ behavior compared to that for a wire which had received a fourth extrusion, as shown in Figure 3.2. Below 4 T the three-extrusion wire had higher critical current densities, while above 5 T the reverse was seen. As we could detect no difference in the average pin thickness or the pin thickness distribution at the optimum flux pinning size ($d_p$=40 nm) for either composite, we

attributed the difference in behavior to pin/matrix interdiffusion caused by the fourth extrusion. Since interdiffusion should reduce the pin proximity length by alloying the Nb, this should lead to the elementary pinning force reaching its peak for thinner pins [52], thus raising the density of pins at maximum $f_p$, and enhancing the bulk pinning force at higher fields where higher $J_c$ is most desirable. However, such interdiffusion should also diminish the composition gradient at the pin/matrix interface, thereby decreasing the strength of $f_p$. Thus interdiffusion can have two opposing effects, making the quantitative impact on $J_c$ unpredictable.

## 4.1 Experimental design

In order to directly address the influence of the sharpness of the pinning well on the strength of $f_p$, we fabricated a new, nominally identical Nb 47 wt.% Ti/Nb APC composite but this time using lower temperature processing. We reduced the number of warm extrusions from four to three and the temperature of the last extrusion from 650 $^o$C to 250 $^o$C. The composite was fabricated using the rod-based technique. Table 4.1 summarizes the fabrication details for this composite. Thirty-one 1 mm diameter rods of Nb were arranged in a hexagonal array within 96 rods of Nb 47 wt.% Ti, such that the center-to-center pin spacing was 1.82$d_p$. The hexagonal-shaped 127 rod stack was canned in Cu, evacuated and hydrostatically warm extruded at 650 $^o$C using a 15:1 area reduction ratio. The extruded wire was cut into 127 filaments, the Cu was etched off and the hexagonal-shaped filaments were re-stacked, canned in Cu and extruded under the same conditions. A third stack of 55 filaments was extruded at 250 $^o$C using a 10:1

66

Table 4.1: APC composite design and fabrication details.

| Matrix composition (wt.% Ti) | APC composition | $V_p$ | $D_c$ (g/cm$^3$) | $n_p/n_{e1}$ | $n_{e2}$ | $n_{e3}$ | $n_{e4}$ | $R$ |
|---|---|---|---|---|---|---|---|---|
| 47 | Nb | 0.244 | 6.63 | 31/127 | 127 | 55 | 7[a] | 1.77 |
| $T_e$ (°C) → | | | | 650 | 650 | 250 | … | |

[a]cold drawn, 7-filament composite.

area reduction ratio. This final warm extrusion brought the nominal pin diameter down to 1.3 μm. The resulting wire was re-stacked with the Cu left on so as to produce a wire with seven superconducting filaments, each filament containing 31×127×55 pinning centers. This wire was drawn to various sizes down to 0.08 mm diameter.

## 4.2  Results

Figure 4.1(a) shows a transverse cross-section of the APC wire at $d_p$=400 nm. Each of the seven superconducting filaments shown contains 216,535 Nb pinning centers, several of which are shown in the accompanying field-emission scanning electron micrograph (secondary electron image) of Figure 4.1(b). The contrast between the Nb and Nb 47 wt.% Ti was obtained by lightly etching with a mixture of 25% $HNO_3$, 25% HF and 50% $H_2O$. At this size, the nominally round pins have started to deform into ribbons but the designed hexagonal symmetry of the pinning center array is still evident. The transmission electron micrograph of Figure 4.1(c) reveals that by $d_p$=25 nm (slightly smaller than the optimum flux pinning size of $d_p$=39 nm) the round pins have transformed into ribbons whose thickness ranges rather broadly from ~1 to 15 nm. This ribbon-shape range parallels that observed in the earlier composite of chapter 3.

Figure 4.2 shows $J_c$ as a function of the nominal pin diameter at applied magnetic fields of 2–7 T for the two prior composites having three and four extrusions respectively and for the new three-extrusion composite. The new composite achieves significantly larger values of $J_c$. Progressive peaks in $J_c(d_p)$ can be seen at 42, 35, 29, 25
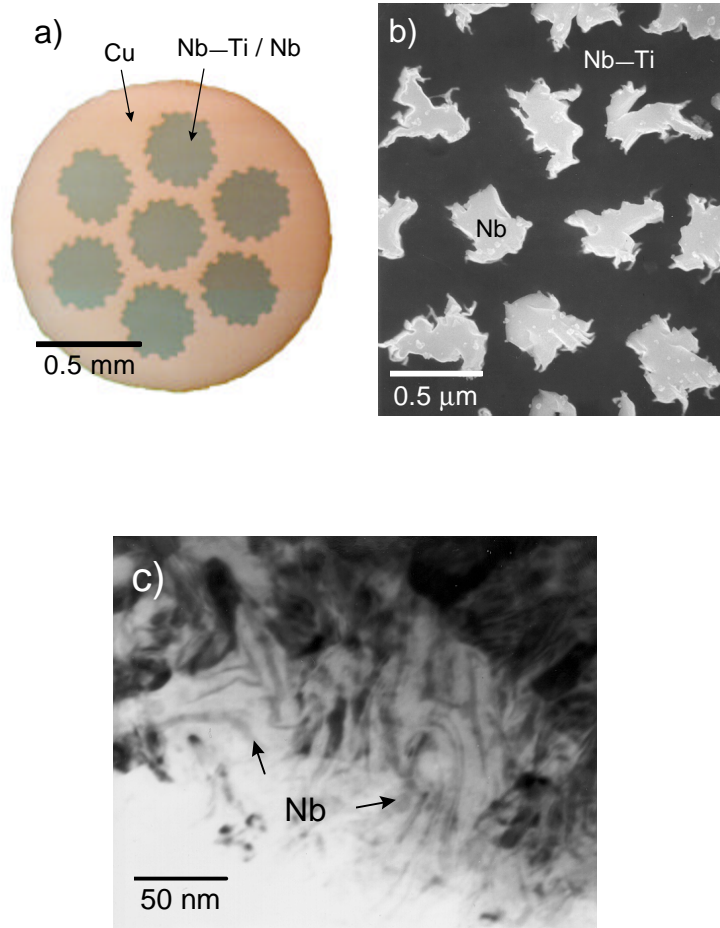
Figure 4.1: (a) Transverse cross-sectional view of the Nb-pin APC wire at a nominal pin diameter of ~400 nm. Each of the seven filaments shown contains 216,535 pinning centers, several of which are shown in the FESEM micrograph of (b). At this size, still a factor of ten larger than the optimum flux pinning size, the round pins are beginning to change shape. By optimum size ($d_p$=25 nm), shown in the transmission electron micrograph of (c), the pins have transformed into ribbons with a broad thickness range of ~1–15 nm (Figure 4.1(c) courtesy of Dr. P.J. Lee).

and 20 nm for fields of 2, 3, 4, 5 and 6 T, respectively. Higher field peaks above 6 T were not observed because wires with $d_p<19$ nm were not fabricated due to a lack of strain space. The data in Figure 4.2 makes it appear that some further high field increase is possible. The $J_c$ properties establish a new benchmark value of 4600 A/mm$^2$ at 5 T, 4.2 K for any round wire of Nb-Ti alloy.

## 4.3  Discussion

Comparison of the properties of the new and the older composites makes it clear that relatively modest changes in the thermomechanical treatment can exert a large effect on the $J_c(d_p, H)$ behavior. The dashed lines show the $J_c(d_p)$ behavior at 3, 5 and 7 T for our earlier Nb 47 wt.% Ti / 24 vol.% Nb pin composites. The data from $d_p$=105–40 nm are from the composite which received three 650 $^o$C extrusions; they follow the data of the new composite well, $J_c$ rising as the pin size decreases to 40 nm. The data sets from $d_p$=60–15 nm show that the earlier four-extrusion composite actually outperforms the new three-extrusion composite at larger pin diameters. However, the new composite outperforms the older one at all fields at smaller pin sizes. This seems to indicate that any potential benefit to the elementary pinning force caused by interdiffusion decreasing the pin proximity length is outweighed by a decrease in the sharpness of the pinning wells. However, a recent experiment [93] described in chapter 6, shows that the pin proximity length does influence the flux pinning behavior, though the full details of its influence are not yet clear.
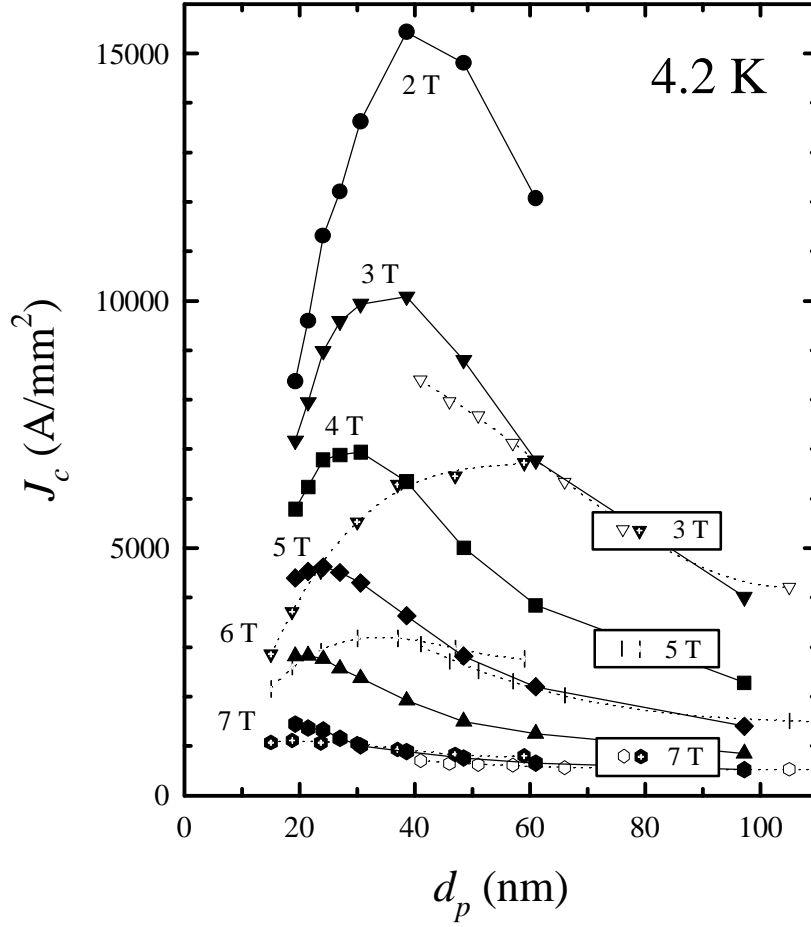
Figure 4.2: $J_c$ as a function of $d_p$ at applied fields from 2–7 T for the Nb-pin APC composites at 4.2 K. The filled symbols connected by continuous lines represent the present composite for which the last extrusion temperature was reduced. The smaller symbols connected by dashed lines are $J_c(d_p)$ data at 3, 5 and 7 T taken from the previous composite which had the same composition of Nb 47 wt.% Ti with 24 vol.% Nb pins, but had received higher temperature processing. Two data sets are shown, that from $d_p$=105–40 nm (open symbols) corresponds to a third extrusion composite, while that from $d_p$=60–15 nm (crossed symbols) corresponds to a fourth extrusion composite.

In any case, the processing refinements embodied in this new composite have significantly contributed to producing a critical current density at 5 T of 4600 A/mm$^2$, a value some ~10% higher than the previous benchmark developed in a multilayered planer Nb pin/Nb 50 wt.% Ti composite [32], despite the present composite containing ~15% less pinning center.  The similarity in high-$J_c$ performance between composites of dissimilar design warrants a direct comparison, since such a comparison may provide insight into the possible role that the starting pin geometry has on the bulk pinning force developed by the final nanostructures.  Figure 4.3 compares $J_c(H)$ for each composite; the values shown correspond to peak values taken from the $J_c(d_p)$ curves of Figure 4.2 and the data of Matsumoto et al. [32].  The $J_c$ properties are almost identical, the properties of present round-pin composite being slightly better at higher field.  The small difference in $J_c(H)$ at high field could arise from slight differences in pin fraction (24% vs. 27%), matrix composition (47 wt.% Ti vs. 50 wt.%) and/or thermomechanical treatment.

However, a much larger disparity exists between the nominal pin dimensions at which maximum $J_c(H)$ occurs.  As shown in lower half of Figure 4.3, the nominal pin diameter at maximum $J_c$ is a factor of 2.5 smaller for the multilayered planar-pin composite.  This disparity can be reconciled by considering the relationship between the number density of pinning interactions $N$ and $d_p$ for each pin geometry, since it is $N$ that is important in the context of pinning force summation.  For round [94] and planar [95] pinning centers, the number density of pinning interactions in the perpendicular field orientation is given by:

$$N \cong 1/(d_s a_0^2) \qquad (d_s \leq a_0) \qquad \qquad (4.1)$$

where $d_s$ is the pin spacing. Thus it is $d_s$ rather than $d_p$ that determines $N$. For 24 vol.% of round pins the average pin spacing $\overline{d}_s$:

$$\overline{d}_s \approx d_p \big/ 12V_p^2 = 1.4 d_p \qquad \qquad (4.2a)$$

while for 27 vol.% of planar pins,

$$\overline{d}_s \approx d_p \big/ V_p = 3.7 d_p \qquad \qquad (4.2b)$$

This analysis shows that for a given pin dimension $d_p$, $d_s$ is approximately 2.6 times larger for the planar pin array; this difference accounts for the entire offset in $d_{pmax}$ between the two composites.

Since the real pin morphology deviated substantially from design as the size approached nanometer dimensions [Figure 4.1(c)], the above analysis is appropriate for discussing only relative differences in the pin density between the two APC designs. Implicit in this analysis is that the pin shape transformed from regular to ribbon-in the same manner for both designs. This is a valid assumption since both composites received similar axially symmetric deformation processing. Determination of the real pin density requires detailed measurement of the final size microstructure, such as that performed by Meingast, Lee and Larbalestier for optimized, conventional Nb 48 wt.% Ti [23]. Such a detailed quantitative analysis was not possible in this study.
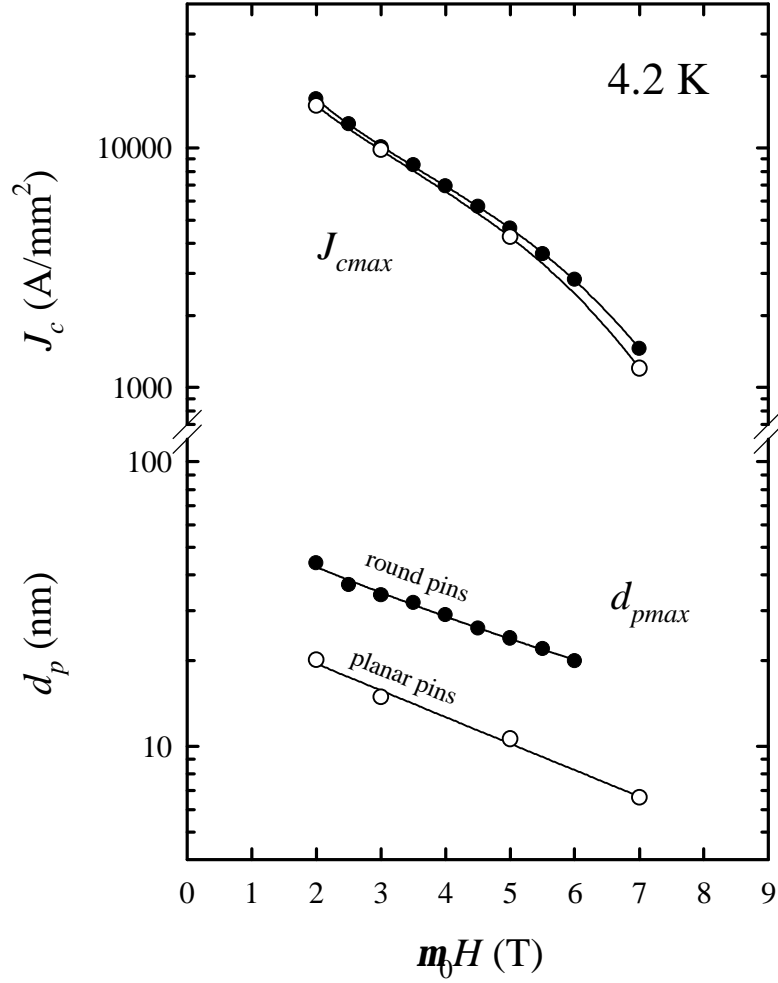
Figure 4.3: Peak $J_c$ ($J_{cmax}$) and nominal pin dimension $d_p$ at which the peak occurred ($d_{pmax}$) as a function of applied field for the present round Nb-pin wire (open circles) and a Nb 50 wt.% Ti wire with 27 vol.% of multilayered planar Nb pins (closed circles) at 4.2 K. The pin dimension $d_p$ in the latter composite refers to the nominal Nb layer thickness.

The final shape and thickness distribution of the pins is likely to be very important in determining the flux pinning properties because of the influence that these parameters exert on the proximity coupling of the pins to the matrix. Round Nb pins change shape drastically in ways dictated by the deformation characteristics and the grain structures of the pin and matrix materials. Even with the additional processing refinements of this study, the pin thickness at optimum size varied from ~1–15 nm, a broader range than is observed in conventional Nb-Ti. Broad pin thickness distributions, such as those found in PMAPC wires with Nb pins [39] and inhomogeneous conventionally processed Nb-Ti [96], are believed to be detrimental to $J_c$. Thus further significant increases in $J_c$ should be possible from more uniform artificial pinning structures, as is suggested by recent multilayer studies by McCambridge et al. [97] and Kadyrov, Gurevich, and Larbalestier [98].

It is important to note that the $J_c$ improvements in the new Nb-pin composite were realized in the absence of any added improvement to $H^*$. At the maximum $J_c$(5 T) size ($d_p$=25 nm), $H^*$ determined by both magnetization and extrapolation of $F_p \rightarrow 0$ was ~9.2 T, essentially the same value as that interpolated from the data of Table 3.2 for our previous round Nb-pin composite. Thus applying a similar normalization correction to $J_c$ of ~45% to the present composite yields $J_c$(5 T, $m_0H^*$=10.7 T)=6600 A/mm$^2$. This value is 80% higher than the best conventionally processed Nb-Ti wire. Clearly there is every incentive to maximize $H^*$, $H_{c2}$ by designing the overall Nb-pin/Nb-Ti for maximum $H_{c2}$,

in accordance with the hypothesis of Meingast, Lee, and Larbalestier [23]. Such an experiment provides the basis for chapter 5.

## 4.4 Conclusions

The critical current density of Nb 47 wt.% Ti wires with 24 vol.% of nominally round artificial Nb pinning centers were studied as a function of pin diameter and magnetic field. Very high $J_c$ values were obtained when interdiffusion between pin and matrix was minimized by using lower temperature thermomechanical processing. A high $J_c$(5 T, 4.2 K) for round wire of 4600 A/mm$^2$ was achieved for a nominal pin diameter of 25 nm, despite the absence of any added improvement to the irreversibility field. Transmission electron microscopy showed that the real pin shape was ribbon-like with a thickness which varied from ~1–15 nm.

# 5. Effect of Nb-Ti matrix composition

This chapter discusses APC composites designed to address the depressed $H_{c2}$ and $H*$ values observed in our previous APC composites composed of Nb 47 wt.% Ti with 24 vol.% Nb pins. As shown in chapter 4, $J_c$ was increased by ~40% in wires with pure Nb pins through only modest changes in the thermomechanical treatment. These improvements were realized in the absence of any added improvement to $H*$ or $H_{c2}$. Since $J_c$ generally scales with $H_{c2}$ and it is the higher-field $J_c$ that is of greatest interest for high energy physics projects, there is every incentive to attain the highest possible $H_{c2}$ in this system ~11.7 T for Nb 44 wt.% Ti [100].

A study of conventionally processed Nb 47 wt.% Ti wire during its final optimization strain by Meingast, Lee, and Larbalestier [23] explained a simultaneous decrease in $T_c$ and increase in $H_{c2}$ as a kind of electromagnetic "homogenization" as the $a$-Ti precipitate thickness was reduced below $x$. Their hypothesis explains the depressed $H_{c2}$ found in

Nb-pin composites as resulting from an overall composite mixture which departs from Nb 44–48 wt.% Ti, the range of composition for which maximum $H_{c2}$ occurs. Thus the goal of this study was to test the hypothesis for Nb-pin APC composites designed for optimum $H_{c2}$ in the coupled limit.

## 5.1 Experimental design

Two APC wires with 24 vol.% Nb pins were fabricated according to the exact specifications given for the Nb 47 wt.% Ti/Nb composite described in chapter 4, a singular difference being the selection of more Ti-rich matrix compositions in order to shift the overall Nb-Ti/Nb composition closer to Nb 44 wt.% Ti in the fully proximity-effect coupled limit. For this purpose, Nb 52 wt.% Ti and Nb 62 wt.% Ti were chosen based on the availability of high homogeneity, low impurity concentration alloy rods custom made for the thesis study of McKinnell [77]. Nb-Ti /Nb overall compositions (OC) in wt.% Ti were calculated using:

$$OC = MC \frac{D_m (1 - V_p)}{D_p V_p + D_m (1 - V_p)}, \tag{5.1}$$

where MC is the Nb-Ti composition in wt.% Ti, and $D_p$ and $D_m$ are the mass densities of the pin and Nb-Ti matrix, respectively. Values of $D_p$, $V_p$, OC, and $H_{c2}$ for each overall composition, as measured by magnetization [100], are listed in Table 5.1 for each composite. As shown in Table 5.1, Nb 52 and 62 wt.% Ti with 24 vol.% Nb correspond to overall compositions of 35 and 42 wt.% Ti, respectively, and thus, in the fully coupled

Table 5.1: Composite density, overall composition (OC), and $H_{c2}$ values.

| Matrix composition (wt.% Ti) | $V_p$ | $D_m$ (g/cm$^3$) | $D_c$ (g/cm$^3$) | OC (wt.% Ti) | $m_0 H_{c2}$ [100] (T) |
|---|---|---|---|---|---|
| 47 | 0.244 | 6.02 | 6.63 | 33 | 10.4 |
| 52 | 0.244 | 5.77 | 6.44 | 35 | 10.6 |
| 62 | 0.244 | 5.52 | 6.25 | 42 | 11.6 |

limit, should develop significantly higher $H_{c2}$ than the previous Nb-pin composite design. Table 5.2 summarizes the fabrication details for this set of composites.

$H_{c2}$ and $H^*$ were measured only for the Nb 47 and 62 wt.% Ti 7-filament composites. During the course of magnetization measurement on the present sample set, we discovered that our previous analysis of $M(H)$ for APC wires, discussed in chapter 3, had incorrectly defined a measurement artifact associated with a small axial offset of the sample position with respect to the Helmholtz coil pair as $H^*$. In turn, $H^*$ had been incorrectly defined as $H_{c2}$. Exacerbating this problem was that the real $H_{c2}$ transition, characterized by a minute increase in the slope of the reversible magnetization, was seldom discernible above the background noise. In the present study, the difficulty in measuring $H_{c2}$ was alleviated by increasing the sample volume, and hence the moment, by a factor of ~5 in order to better resolve the $H_{c2}$ transition. The Cu matrix was chemically removed in order to increase the superconductor fill factor and also to remove a small temperature-dependent diamagnetic contribution from the copper. As in our previous magnetization study, the sample length was maximized

in order to insure that the magnetization correlated to $J_c$ flowing parallel to the pins ($J_{c\parallel}$) rather than $J_c$ crossing the pins at each end of the wire ($J_{c\perp}$). Small (<0.3 mm) diameter wires were wound into 3 mm diameter, 2 mm tall open-circuit coils encased in Duco cement. However, this geometry was not feasible for the two largest diameter wires (1 and 0.3 mm dia.). Fortunately, these large-diameter wires had correspondingly large-diameter pins and thus low pin densities, low $J_{ct}$, and low $J_{c\parallel}/J_{c\perp}$ anisotropy. In every case where $J_{cm}$ could be compared to $J_{ct}$, there was close agreement, thus providing a strong indication that the longitudinal critical current density, corresponding to $J_{ct}$, determined **DM** and thus $H^*$.

## 5.2  Results

Figures 5.1(a)–(c) plot the bulk pinning force $F_p(H)$ curves as a function of the nominal pin diameter for the Nb 47, 52, and 62 wt % Ti-matrix Nb-pin composites, respectively. One similarity between the three composites is the absence of low field data for the larger pin wires. This is a consequence of having wires with high-$J_c$ and rather large diameter (>50 μm) filaments, a combination which caused flux jumping [56] to the normal state at transport currents well below $I_c$. Flux jumping was suppressed as the wire diameter was further reduced.

A second similarity between the three composites is shown by their qualitatively similar $F_p(H)$ development with decreasing pin diameter. As $d_p$ was reduced below 100 nm, a low-field peak in $F_p(H)$ emerged, while the magnitude of $F_p$ increased at all

Table 5.2: APC composite design and fabrication details.

| Matrix composition (wt.% Ti) | APC composition | $V_p$ | $D_c$ (g/cm$^3$) | $n_p/n_{e1}$ | $n_{e2}$ | $n_{e3}$ | $n_{e4}$ | $R$ |
|---|---|---|---|---|---|---|---|---|
| 47 | Nb | 0.244 | 6.63 | 31/127 | 127 | 55 | 7[a] | 1.77 |
| 52 | Nb | 0.244 | 6.44 | 31/127 | 127 | 55 | 7[a] | 1.90 |
| 62 | Nb | 0.244 | 6.25 | 31/127 | 127 | 55 | 7[a] | 1.59 |
| $T_e$ (°C) $\rightarrow$ | | | | 650 | 650 | 250 | ... | |

[a] cold drawn, 7-filament composite.

fields. At $d_p \sim 35$ nm a maximum $F_p(H)$ of 28–32 GN/m$^3$ is observed at 2–3 T. Both $H_{max}$

and $F_{pmax}$ decreased slightly with increasing Ti content. While the overall development

of $F_p(H, d_p)$ is very similar for the three composites, a significant difference in behavior

can be observed at higher fields. For the Nb 47 wt.% Ti-matrix composite, $F_p(H, d_p)$

saturated [99] at a field slightly lower than $H_{c2}$, despite a shift in $H_{max}$ toward higher field

as the nominal pin diameter was reduced. Similar saturation behavior is observed for the

Nb 52 wt.% Ti-matrix composite although, in this case, saturation occurred closer to

$H_{c2}$, as shown in Figure 5.2(b). However, no saturation of $F_p(H, d_p)$ is observed for the

Nb 62 wt.% Ti-matrix composite [Figure 5.1(c)]. Moreover, the extrapolation of $F_p \to 0$

(a second method commonly used to define $H^*$) appears to *increase* slightly as opposed

to the decrease observed in for the Nb 47 and 52 wt.% Ti-matrix composites.


Figure 5.2 shows a $M(H)$ curve for a typical APC wire at 4.2 and 6 K in the field

region near $H_{c2}$. Small paramagnetic and diamagnetic contributions from the Nb-Ti and

quartz sample rod, respectively, are responsible for the paramagnetic magnetization

above $H_{c2}$. $H^*$ is defined as the field where the hysteretic magnetization tends to zero;

$H_{c2}$ is defined as the field at which the reversible magnetization changes slope, becoming

coincident with a $M(H)$ loop made at a slightly higher temperature. Both constructions
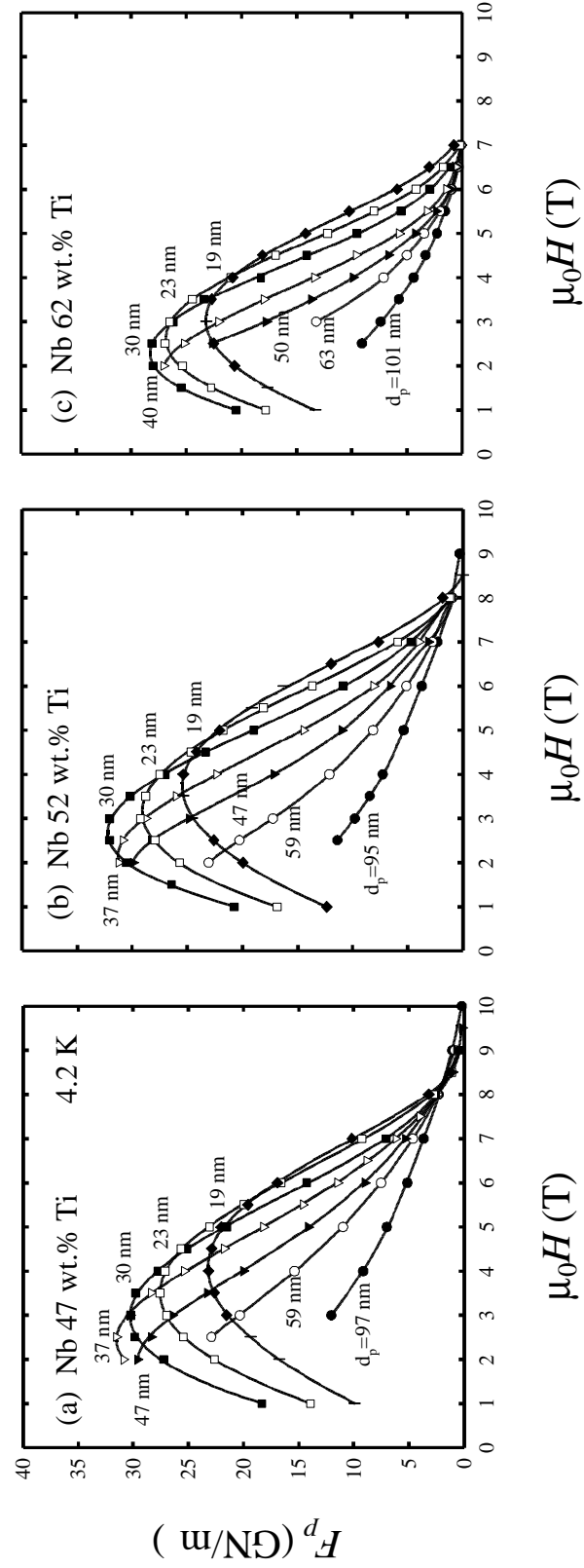
are illustrated in Figure 5.2.

Figure 5.1: $F_p(H)$ as a function of $d_p$ for the (a) Nb 47 wt.% Ti, (b) Nb 52 wt.% Ti, and (c) Nb 62 wt.% Ti-matrix composites at 4.2 K. Saturation of $F_p(H)$ can be observed above 8 T in (a) and (b), but not in (c).
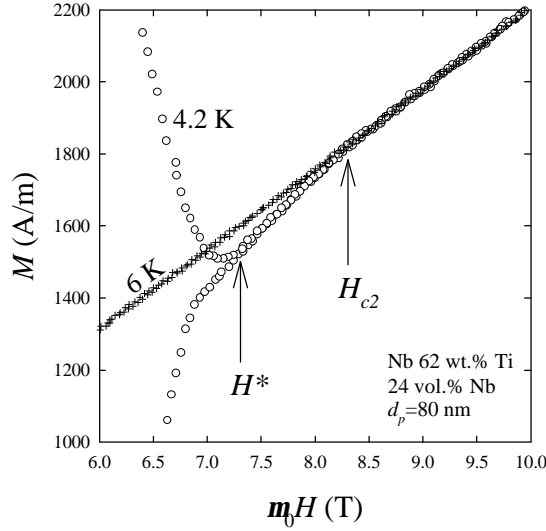
Figure 5.2: *M(H)* curve for an APC wire at 4.2 and 6 K in the field region near $H_{c2}$. Small paramagnetic and diamagnetic contributions from the Nb-Ti and quartz sample rod, respectively, are responsible for the paramagnetic magnetization observed above $H_{c2}$. *H\** is defined as the field where the irreversible magnetization goes to zero; $H_{c2}$ is defined as the field at which the reversible magnetization changes slope, becoming coincident with a *M(H)* loop made at 6 K.

Figure 5.3 plots the magnetization $H_{c2}$ and *H\** as a function of $d_p$ for the Nb 47 and 62 wt.% Ti-matrix, 7-filament composites. Also included are *H\** values defined by extrapolation of $F_p(H) \rightarrow 0$, hereupon referred to as $H^*_{Fp \rightarrow 0}$. Data from an optimized, conventionally processed Nb 47 wt. Ti wire [100] are shown for comparison, the values of $d_p$ for this wire were calculated from the average *a*-Ti precipitate diameter of 150 nm, following the final precipitation heat treatment [22]. For the Nb 47 wt.% Ti-matrix APC composite, $m_0 H_{c2}$ decreased from 12–10.5 T and $m_0 H^*$ from 11.5–9 T as the nominal pin diameter was reduced from ~1 μm to 20 nm. $H^*_{Fp \rightarrow 0}$ is in good agreement
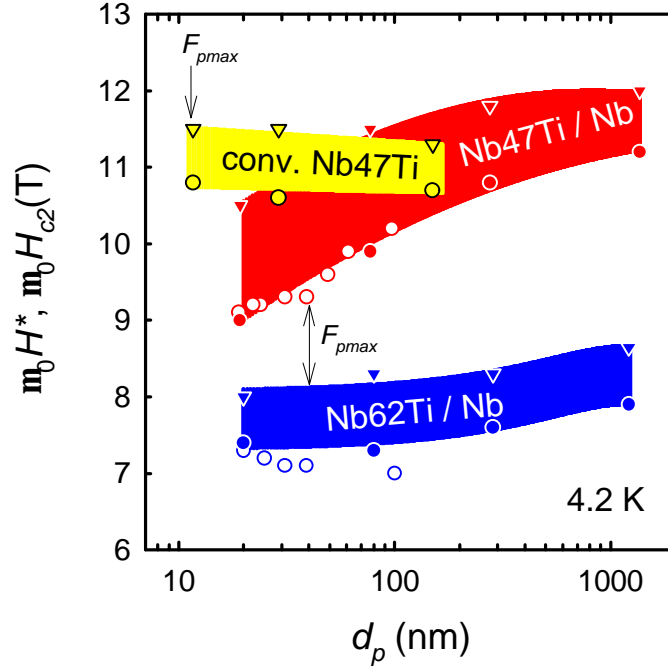
Figure 5.3: Magnetization upper critical field (triangles) and irreversibility field (filled circles) as a function of nominal pin diameter at 4.2 K for the Nb 47 and 62 wt.% Ti-matrix APC wires as well as a conventionally processed Nb 47 wt.% Ti wire [100]. For the conventional wire, $d_p$ is calculated using the 150 nm average precipitate size at $e$=0. The open circles correspond to extrapolations of $F_p \rightarrow 0$.

with $H^*$ determined from magnetization. Over the same interval of $d_p$, the Nb 62 wt.% Ti-matrix composite showed a similar but less severe decline both $H_{c2}$ and $H^*$, $m_0H_{c2}$ decreasing from 8.7–8 T and $m_0H^*$ from 7.9–7.4 T. However, in this case both $H^*$ and $H^*_{Fp \rightarrow 0}$ increased as $d_p$ decreased from 80 to 20 nm.

The conventionally processed Nb 47 wt.% Ti wire exhibited a slight increase in $m_0H_{c2}$ from 11.2–11.5 T, while $m_0H^*$ remained essentially constant (10.7 T) during the final

optimization strain, corresponding to a decrease in $d_p$ from 150–10 nm. The vertical arrows in Figure 5.3 indicate the nominal pin diameters at which each composite reached their maximum value of $F_p$ ($F_{pmax}$). $F_{pmax}$ occurred at $d_p$~40 nm for both Nb-pin composites while for the conventional wire $F_{pmax}$ occurred at $d_p$~10 nm; the actual pin thickness at these sizes ranged from ~1–20 nm and 1–5 nm, respectively.

## 5.3  Discussion

### 5.3.1  Microstructural development

Although no electron microscopy is presented for the Nb 52 and 62 wt.% Ti-matrix composites, their pin arrays were observed by FESEM at intermediate pin diameters of ~500 and 100 nm. The degradation in pin shape appeared to proceed in identical fashion to that for the Nb 47 wt.% Ti composite, as shown in Figure 4.1(b) and a similar trend was expected down to the optimum flux pinning range of $d_p$=100–20 nm. This is a reasonable assumption, since any deviation in the pin shape from that of the Nb 47 wt.% Ti-matrix composite should have commenced at a much earlier stage in processing. It should be noted that ~1–3 volume percent of equiaxed *a*-Ti precipitate was observed in FESEM performed on the Nb 62 wt.% Ti-matrix composite following its last extrusion; no precipitation was detected in the Nb 47 and 52 wt.% Ti-matrix composites. This is not surprising since the nucleation and growth kinetics for *a*-Ti precipitation increase rapidly with increasing Ti content. However the precipitate diameter of 30–50 nm was ~50 times smaller than the pin diameter at this size, and thus were inconsequential to the

$F_p(H)$ curves of Figure 5.1(c).  Therefore, all further discussion of the Nb 47, 52 and 62 wt.% Ti-matrix composites will assume nanostructural consistency.

*5.3.2  H\* and $H_{c2}$ vs. $d_p$*

Taken together, Figures 5.1 and 5.3 clearly show the trends in *H\** and $H_{c2}$ with decreasing $d_p$.  For the Nb 47 wt.% Ti-matrix composite, the Nb pins appear to be fully coupled to the matrix by $d_p$=20 nm:  the $m_0 H_{c2}$ of 10.4 T is equal to the value given in Table 5.1 for the overall composite mixture of Nb 33 wt.% Ti.  However the Nb 62 wt.% Ti-matrix composite only developed $H_{c2}$=8 T by $d_p$=20 nm, well below the value of 11.6 T predicted in the fully coupled limit.

In light of this somewhat surprising result, two additional containing Nb 47 and 62 wt.% Ti-matrix composites were fabricated to explore further changes in *H\** and $H_{c2}$ at finer pin diameters than the 7-filament architecture allowed.  The new wires were fabricated from the same monofilamentary stock used for the 7-filament conductors, the only difference being that 55-filament wires were made by low (250°C) temperature extrusion rather than cold drawing.  Whereas the 7-filament composites provided a final nominal pin diameter of 19 nm, the 55-filament composites provided $d_p$=7 nm. Extrapolation of pin thickness measurements made at $d_p$~25 nm [Figure 4.1(c)] down to $d_p$=7 nm, yields a thickness range of <<1–2 nm, well below the 5 and 6 nm coherence lengths of Nb 47 and 62 wt.% Ti, respectively.
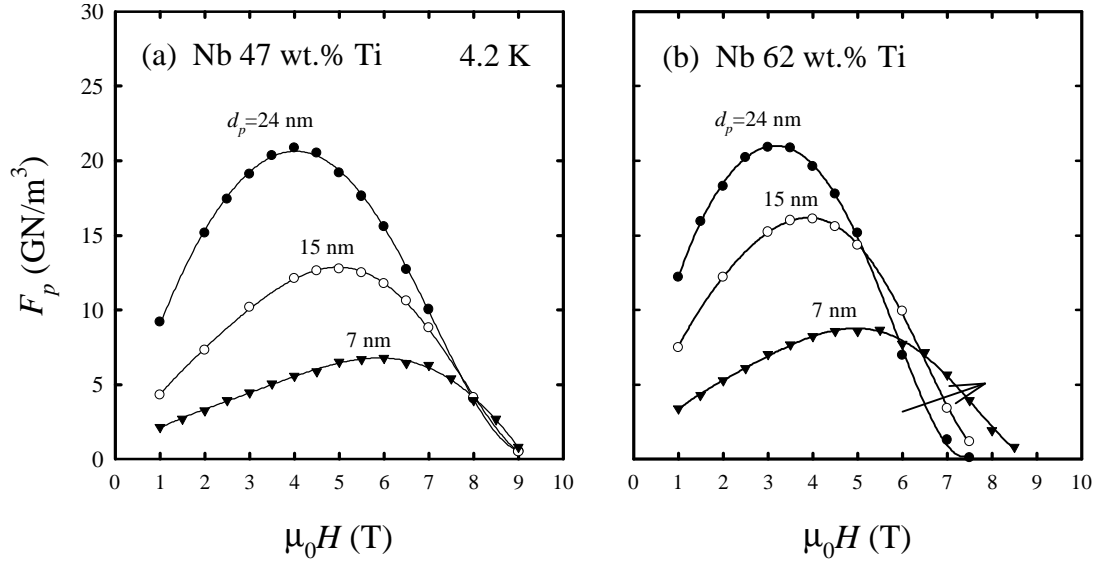
Figure 5.4: $F_p(H)$ as a function of $d_p$ for the (a) Nb 47 wt.% Ti and (b) Nb 62 wt.% Ti-matrix, 55-filament composites at 4.2 K. The arrow in (b) indicates a significant increase in $H^*_{Fp \to 0}$ with decreasing $d_p$.

Figures 5.4(a) and (b) plot $F_p(H)$ as a function of $d_p$ for the Nb 47 and 62 wt.% Ti 55-filament composites as a function of $d_p$. These two curves should be considered extensions of the curve sets shown in Figures 5.1(a) and (c). The trend of increasing $H_{max}$ with an accompanying decrease in $F_{pmax}$ continued for both composites, although the decline $F_{pmax}$ is less rapid for the Nb 62 wt.% Ti-matrix composite. The enhanced pinning in the Nb 62 wt.% Ti likely originates from ~8–10 vol.% of **a**-Ti precipitate that was produced during the fourth extrusion. Unlike the case described earlier for the 7-filament composite, here the **a**-Ti precipitates were only ~10 times smaller than the Nb artificial pins, and thus may have contributed some pinning to the bulk pinning force curves shown in Figure 5.4(b).

Examination of $F_p(H)$ near $H_{c2}$ for the Nb 47 wt.% Ti-matrix composite shows saturation of $F_p(H)$ above 8 T and $H^*_{Fp\to 0}$ ~9 T, exactly the behavior observed in Figure 5.1(a) as $d_p$ approached 19 nm and further validation that the pins are fully coupled to the matrix.  For the Nb 62 wt.% Ti-matrix composite, $H^*_{Fp\to 0}$ increased from 7.5 to 8.7 T as $d_p$ decreased from 24 to 7 nm.  Although the 1.2 T enhancement in $H^*$ is significant, it is still 3 T lower than the predicted $m_0H_{c2}$ of 11.6 T.  In light of the discrepancy between the behavior expected from the phenomenological predictions of Meingast, Lee, and Larbalestier, and the behavior observed for the Nb-pin wires, an analysis of proximity effect theory is necessary.

### 5.3.3  Proximity effect theory

Proximity-effect theory [42, 43, 45, 46] describes the behavior of dirty-superconductor–normal-metal (S/N) bilayers as the bilayer period approaches the coherence length $x$. Microscopically the proximity effect involves diffusion of superelectrons from the superconductor into the normal metal.  A decrease in the layer thicknesses is generally accompanied by a decrease in $T_c$ and/or $H_{c2}$, the magnitude of which is dictated by the respective layer thicknesses and proximity lengths.   In the context of traditional proximity-effect theory, no increase in $T_c$ or $H_{c2}$ is considered.

However, in the Nb-Ti system, as well as other superconducting alloy systems such as Nb-Zr and Nb-Ta, the alloy is a stronger superconductor than the pure element constituents.   Thus in the limit of infinitesimal bilayer period, the superconducting

properties should approach the higher properties of the homogenous mixture. This has been observed experimentally in studies of pure Nb/Ti thin film multilayers by Sato [101], Qian et al. [102], and Warnes, Faase, and Norris [103, 104]. In each of these cases, traditional proximity effect theory fails to properly describe the superconducting properties in the limit of infinitesimal layer thicknesses. In order to address this obvious shortcoming of traditional proximity-effect theory Ledvij, Dobrosavljevij-Grujic, and Clem [105] developed a trilayer model to describe the behavior of Nb/Ti multilayer films with decreasing layer thickness. They modeled the Nb/Ti films as superconductor-*interphase*-normal-metal (*S*/*I*/*N*) multilayers, for which the alloy Nb-Ti interphase layer accounts for interfacial roughness or mixing of Nb and Ti due to interdiffusion. As the trilayer period decreases, the interphase Nb-Ti layer accounts for an increasingly large fraction of the trilayer, dominating the behavior at infinitesimal bilayer periods. This model accurately described the initial decrease and then subsequent increase in $T_c$ for the Nb/Ti multilayers of Qian et al. [102] as the bilayer period was reduced from 200 to 1 nm.

Thus, a fundamental difference exists between the phenomenological proximity "mixing" model proposed by Meingast, Lee, and Larbalestier and the trilayer proximity-effect model developed by Levij et al. Within the framework of the former model, the *coherence length* is the characteristic length scale which governs the $T_c$ and $H_{c2}$ in the fully coupled limit, while in the latter model, the volume fraction of *interphase* layer determines the properties. It appears that the latter model more accurately describes the

properties of the Nb 62 wt.% Ti-matrix composite. Since the thermomechanical processing in the present composites were tailored to minimize pin-matrix interdiffusion, the interphase layer should be very thin. This is a reasonable, but so far purely schematic explanation for why $H_{c2}$ and $H^*$ in the Nb 62 wt.% Ti composite did not nearly approach the values calculated for the homogeneous alloy, despite the average pin thickness being much less than the coherence length. Extending this argument, the decrease in $H_{c2}$ observed in Figure 5.3 for the Nb 47 and 62 wt.% Ti-matrix composites can be attributed to the traditional proximity effect, while the saturation of $H^*_{Fp \to 0}$ shown in Figure 5.4(a) and the slight enhancement of $H^*_{Fp \to 0}$ shown in Figure 5.4(b) can be attributed to the formation of an interphase Nb-Ti layer, as proposed by Ledvij, Dobrosavljevij-Grujic, and Clem [105].

## 5.4 Conclusions

The field-dependent bulk pinning force, upper critical field, and irreversibility field were measured for a set of Nb-pin APC wires with Nb 47, 52 and 62 wt.% Ti-matrices as the nominal pin diameter was reduced from 1 μm to 7 nm. The shape of $F_p(H)$ with decreasing pin diameter was qualitatively the same for all three composites, as was the maximum value of $F_{pmax}$ (28–32 GN/m$^3$). For the Nb 62 wt.% Ti-matrix composite, which was designed for maximum upper critical field in the proximity-effect coupled limit, $H^*$ increased from 7.5–8.7 T as the nominal pin diameter was reduced from 24–7 nm. However, the enhancement was significantly less than predicted for the fully

coupled limit, even when the pins were much thinner than the superconducting coherence length. In the context of a proximity-effect model by Ledvij, Dobrosavljevij-Grujic, and Clem [105], this can be attributed, unfortunately, to the same minimal pin/matrix interdiffusion held responsible for high $J_c$ at low fields.

# 6. Effect of pin proximity length

Based on several inconsistencies of the core pinning mechanism used to describe flux pinning in conventionally processed Nb-Ti wire and the markedly different $F_p(H)$ curves developed in Nb-Ti wires with Nb-artificial pinning centers, (compare Figures 5.1 and 1.8) Cooley, Lee, and Larbalestier [52] proposed that magnetic pinning is the dominant pinning mechanism in both APC and conventional Nb-Ti. They extended the earlier model of Gurevich and Cooley [51] to the characteristic ribbon-shaped pins found in conventional and APC Nb-Ti wire at optimum size, modeling the ribbons as $S/N/S$ junctions with a characteristic transmission current density ($J_p$) defined by their normal-state properties and thickness. In the context of this model, a planar pin behaves similarly to a surface which blocks or diverts supercurrent, creating a large image force that attracts the vortex to the pin. As the vortex approaches the pin, the circulating supercurrent density ($J_s$) can eventually exceed $J_p$. Thus the character of the fluxon is

determined by the magnitude of $J_p$: for $J_p \sim J_s$, there is full transmission of $J_s$ and the vortex behaves as the classical Abrikosov fluxon and experiences no magnetic pinning. Conversely for $J_p=0$, as is the case for a free surface or an insulator, the pinning is purely magnetic and the vortex behaves as a Josephson fluxon. Normal-conducting pinning centers obligate behavior between these two limits, forming fluxons with Abrikosov–Josephson or AJ character.

Within the framework of the magnetic pinning model, both the maximum value of the bulk pinning force $F_{pmax}$ and the corresponding reduced field at which the maximum occurs $h_{max}$ are governed by the pin proximity length ($\textbf{\textit{x}}_N$), given by

$$\textbf{\textit{x}}_N(T) = \left(\hbar \textbf{\textit{u}}_F l / \; 6\textbf{\textit{p}}k_B T\right)^{1/2} \tag{6.1}$$

$$l = \textbf{\textit{u}}_F m / ne^2 \tag{6.2}$$

where $\hbar$ is the modified Planck constant, $\textbf{\textit{u}}_F$ is the Fermi velocity, $k_B$ is Boltzmann's constant, $l$ is the electron mean free path, $m$ is the electron rest mass, $n$ is the number of free electrons per unit volume and $\textbf{\textit{r}}$ is the resistivity.

A key prediction of the magnetic pinning model is that the maximum elementary pinning force should occur for a pin thickness of $\sim\textbf{\textit{x}}_N$. The maximum bulk pinning force is then the best compromise between getting a high $f_p$ and a high $N$, this condition occurring when the thickness is $\sim\textbf{\textit{x}}_N/3$. Thus, the number density of pins at optimum thickness and consequently $h_{max}$, are determined *solely* by the electronic properties of the pin material. Since $\textbf{\textit{x}}_N(\textbf{\textit{a}}\text{-Ti})$ is less than $\textbf{\textit{x}}_N(\text{Nb})$, $h_{max}$ is higher for $\textbf{\textit{a}}$-Ti pins than for Nb

pins. The fact that this is observed experimentally suggests that alloyed Nb pins will exhibit increased values of $h_{max}$.

In order to test these predictions, APC wires with alloyed Nb pins were fabricated, the aims being (1) to reduce the pin proximity length by shortening the electron mean free path and (2) to maintain a Nb-rich composition to allow for comparison with already existing APC composites made with pure Nb pins. The second point is particularly important when considering that pins with crystal structures other than the body centered cubic (bcc) structure of Nb can produce markedly different nanostructures. Both Nb 7.5 wt.% Ta and Nb 10 wt.% W form bcc substitutional solid solutions, exhibit room temperature strain hardening characteristics that are similar to Nb 47 wt.% Ti, and have proximity lengths that are significantly shorter, 30% and 60% respectively, than that of pure Nb. Hence, they make good candidates for artificial pins.

## 6.1  Experimental design

Pin proximity lengths were calculated using Equations 6.1 and 6.2 and the resistivities of 0.23 mm diameter wires measured at 10 K. The pin resistivities were measured in a variable temperature cryostat using a 100 mA current and a 10 cm voltage tap spacing. Although the values of $x_N$ are higher than those established by Cooley et al. [52], no attempt is made here to correct for the simple classical expressions of Equations 6.1 and 6.2.

Table 6.1: APC composite design and fabrication details.

| Matrix composition (wt.% Ti) | APC composition | $V_p$ | $D_c$ (g/cm$^3$) | $n_p/n_{e1}$ | $n_{e2}$ | $n_{e3}$ | $n_{e4}$ | R |
|---|---|---|---|---|---|---|---|---|
| 47 | Nb | 0.244 | 6.63 | 31/127 | 127 | 55 | 7[a] | 1.77 |
| 47 | Nb 7.5 wt.% Ta | 0.25 | 6.74 | 91 | 91 | 55 | 7[a] | 1.65 |
| 47 | Nb 10 wt.% W | 0.25 | 6.78 | 91 | 91 | 55 | ... | 1.5 |
| $T_e$ (°C) → | | | | 650 | 650 | 250 | ... | |

[a] cold drawn, 7-filament composite.

Table 6.1 summarizes the fabrication details for the three APC composites. The Nb-pin APC composite was fabricated using the rod-based APC process and contained 24.4 vol.% of pins [106]. A comprehensive analysis of its microstructure and $J_c$ properties was presented in chapter 4.

The alloyed Nb-pin APC composites were fabricated using the island-type method first described in [27], in which a rod of the pin material is inserted into a hole drilled into a rod of Nb-Ti. In this case the pin diameter was half that of the Nb-Ti rod, yielding a pin volume fraction of 25%. Previous analysis of strain hardening in the Nb 10 wt.% W [107] showed an increased strain hardening compared to that for single-phase Nb 47 wt.% Ti [108]. Therefore, in order to minimize differential hardening between the two materials during reduction, the Nb 10 wt.% W rod was heat treated for 6 hr at 1300 $^{\circ}$C prior to billet assembly. This heat treatment was designed to recrystallize the Nb 10 wt.% W and develop a fine-grained equiaxed grain structure to minimize the type of bcc plane-strain induced shape degradation discussed in chapter 3. In preparation for heat treatment, the Nb 10 wt.% W rod was wrapped in Nb foil and inserted within a 14 mm ID $\times$ 16 mm OD quartz tube, along with a Nb-foil-wrapped titanium getter. The quartz tube was evacuated to $<10^{-3}$ Pa for 12 hr and sealed off under 50 kPa of argon to minimize the evaporation of Ti inside the vessel during heat treatment. After encapsulation, the Ti getter was locally heated to red heat in order to absorb any remaining residual gases. During heat treatment a cover gas of argon was flowed over

the tube in order to maintain an equal oxygen activity on both sides, and thus minimize oxygen diffusion through the quartz.

The Nb 47 wt.% Ti/alloyed Nb-pin composites were canned in Cu and extruded at ~650$^{\circ}$C using an area reduction ratio of 10. The extruded wires were drawn, cut lengthwise into 91 filaments and the Cu was etched off. The filaments were stacked and extruded under the same conditions. The stack and extrusion sequence was followed twice more with 91 and 55 filaments, the final extrusion being made at ~250$^{\circ}$C. The Nb 7 wt.% Ta-pin wire was drawn through a hexagonal shaped die at 1.1 mm and 7 filaments were re-stacked and canned in a Cu tube, the end product being a wire containing 7 superconducting filaments, each filament containing 91×91×55 pinning centers. The Nb 10 wt.% W-pin composite was also designed to be a 7-filament composite, however, during its final extrusion only the front section of the composite billet extruded uniformly and the small portion of good quality wire that resulted had to be drawn down as a monofilament. Each composite was cold drawn to various diameters down to 0.08 mm. Vickers microhardness measurements were made on transverse wire cross sections using 200 g or 1000 g loads applied for 15 s.

## 6.2  Results

Table 6.2 lists the 10 K resistivity, mean free path, and proximity length values for each pin material. The $x_N$ values for Nb, Nb 7 wt.% Ta and Nb 10 wt.% W and pure Ti (included as a reference for $a$-Ti) are 83, 59, 32 and 32 nm, respectively.

Table 6.2: Artificial pin electronic properties at 10 K.

| Pin material | $D_p$ (g/cm$^3$) | $r_0$ ($\mu\Omega$-cm) | $l$ (nm) | $x_N$ (nm) |
|---|---|---|---|---|
| Nb | 8.55 | 0.567 | 53 | 83 |
| Nb 7.5 wt.% Ta | 4.51 | 1.11 | 27 | 59 |
| Nb 10 wt.% W | 9.01 | 3.67 | 7.7 | 32 |
| Ti | 8.80 | 5.61 | 6.1 | 32 |

An analysis of the fractured Nb 10 wt.% W-pin composite following the final extrusion is presented in Figure 6.1. Figure 6.1(a) shows a portion of the as-extruded Nb 10 wt.% W pin wire. Circumferential striations are barely visible at 3 cm intervals along the length of the wire. Figure 6.1(b) shows the same section of wire after the copper sheath was etched away, revealing a highly fractured Nb-Ti/Nb-W core, the fractures forming a succession of tear-drop shaped 1–2 cm long pieces. Figure 6.1(c) shows a graph of extrusion pressure as a function of time recorded for this composite; the periodic core fracture shown in Figure 6.1(b) manifested as periodic spikes in the pressure. The circled portion of the pressure trace indicates a very short interval of uniform deformation near the outset of the extrusion cycle, precisely the short section of monofilamentary wire which was subsequently drawn to final size and characterized.

Figures 6.2(a)–(c) show FESEM secondary-electron micrographs of the Nb, Nb 7 wt.% Ta and Nb 10 wt.% W composites, respectively, at $d_p$~400 nm. At this size, still an factor of ~10 larger than optimum size, the pin shape is irregular but the designed hexagonal pin arrangement is still apparent. The only noticeable difference between the
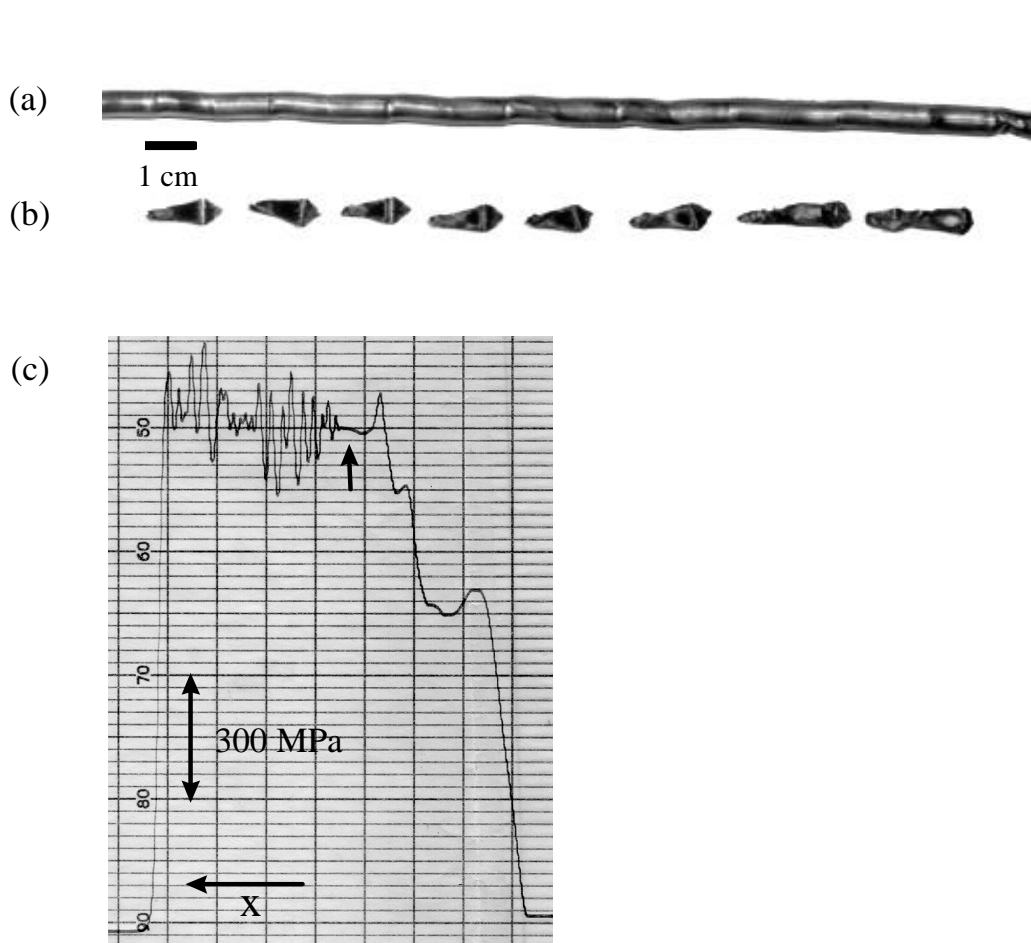
Figure 6.1: Analysis of the fractured Nb 10 wt.% W-pin composite following its final extrusion. Figure 6.1(a) shows a portion of the composite after the final extrusion. Circumferential striations are barely visible at 3 cm intervals along the length of the wire. 6.1(b) shows the same section of wire after the Cu sheath was etched away revealing the highly fractured Nb-Ti/Nb-W core. 6.1(c) shows a graph of extrusion pressure as a function of distance; the periodic fractures shown in (b) are manifested as spikes in the pressure. The vertical arrow in (c) indicates a very short interval of uniform deformation near the outset of the extrusion cycle, precisely the section of wire which was drawn to final size.
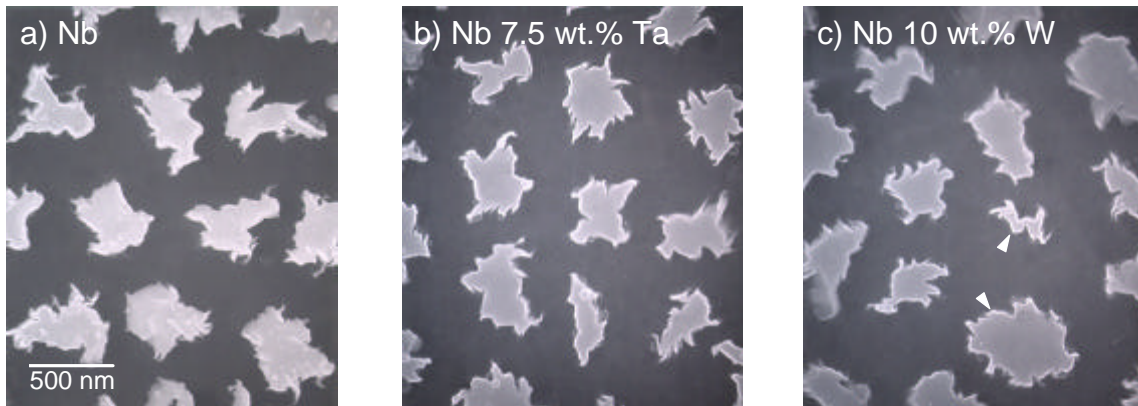
Figure 6.2: FESEM secondary-electron micrographs of the (a) Nb, (b) Nb 7 wt.% Ta and (c) Nb 10 wt.% W pinning arrays at a nominal pin diameter of ~400 nm. The transverse wire sections were lightly etched with a mixture of 25% $HNO_3$, 25% HF and 50% $H_2O$. Examples of sausaged Nb-W pins are indicated by the arrows in (c).

three pin arrays is that some sausaging of the Nb 10 wt.% W pins occurred, as shown in Fig. 6.2(c). This may be partially the consequence of insufficient work-recrystallization cycles for the Nb 10 wt.% W alloy, which had a different origin from the Nb and Nb 7 wt.% Ta.

Figure 6.3 plots the Vickers microhardness as a function of the nominal pin diameter. At larger pin diameters (5 mm > $d_p$ > 50 μm), the pin hardness could be determined, but at smaller diameters (50 μm > $d_p$ > 100 nm) only the composite hardness could be measured. Breaks in the data indicate where the warm extrusions occurred. The strain-hardening characteristics of the Nb and Nb 7 wt.% Ta pins and the Nb 47 wt.% Ti matrix are very similar; the hardness increases with cold drawing strain but drops off
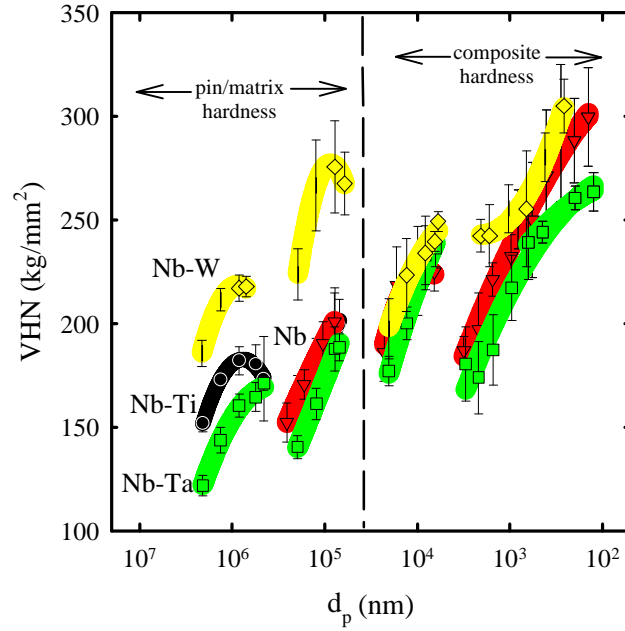
Figure 6.3: Vickers microhardness as a function of nominal pin diameter for the Nb, Nb-Ta, and Nb-W-pin composite wires. Data from 5 mm $> d_p >$ 50 μm reflect the pin or Nb-Ti matrix hardness while those from 50 μm $> d_p >$ 100 nm reflect the overall composite hardness. Breaks between the data sets indicate where the extrusions occurred.

during extrusion. The Nb 10 wt.% W pins strain harden at a rate similar to the other pins but are 50–75 kg/mm$^2$ harder and do not recover during extrusion. As a result, the overall strain hardening rate is higher for both the Nb 10 wt.% W pins and the Nb 10 wt.% W/Nb 47 wt.% Ti composite.

Figures 6.4(a)–(c) plot the bulk flux pinning force as a function of applied field for the three composites. The development of $F_p(H)$ with decreasing pin diameter shown for the Nb-pin composite in Figure 6.4(a) was described in the previous chapter. As the

nominal pin diameter decreased below 100 nm, a low field peak in $F_p(H)$ emerged, reaching a maximum value of 32 GN/m$^3$ at 2.5 T for $d_p$~40 nm. When the pin size was further reduced, the peak position shifted to higher fields, but the magnitude declined. A similar development of $F_p(H)$ with decreasing pin diameter is shown for the Nb 7 wt.% Ta-pin composite in Figure 6.4(b). In this case $F_{pmax}$ reached 25 GN/m$^3$, but at higher field (3 T) and smaller $d_p$ (35 nm). It should be noted that low field flux jumps in the wires with $d_p$>35 nm may have prevented measurement of the true $F_{pmax}$.

The development of $F_p(H)$ over the interval $d_p$=82–32 nm in the Nb 10 wt.% W-pin composite shown in Figure 6.4(c), differs qualitatively from that observed for the pure Nb and Nb 7 wt.% Ta-pin composites. It bears a closer resemblance to the development of $F_p(H)$ seen in conventionally processed Nb 47 wt.% Ti during the drawing strain at large pin size following the last precipitation heat treatment (see Figure 1.8). As in the other APC composites, a low field peak in $F_p(H)$ develops at large $d_p$, but the optimum curve is not reached, at least until $d_p$=32 nm (the smallest wire tested). The peak value of $F_p$, 15 GN/m$^3$, appears to still be rising with decreasing $d_p$ because there is a comparatively larger increase of $F_p$ with changing $d_p$ at this size than is seen in Figures 6.4(a) and (b) near the optimum value of $d_p$.

## 6.3 Discussion

As expected, the proximity length of the Nb pins decreased with alloying. The proximity lengths of Nb 7 wt.% Ta (59 nm) and Nb 10 wt.% W (32 nm) are 30% and
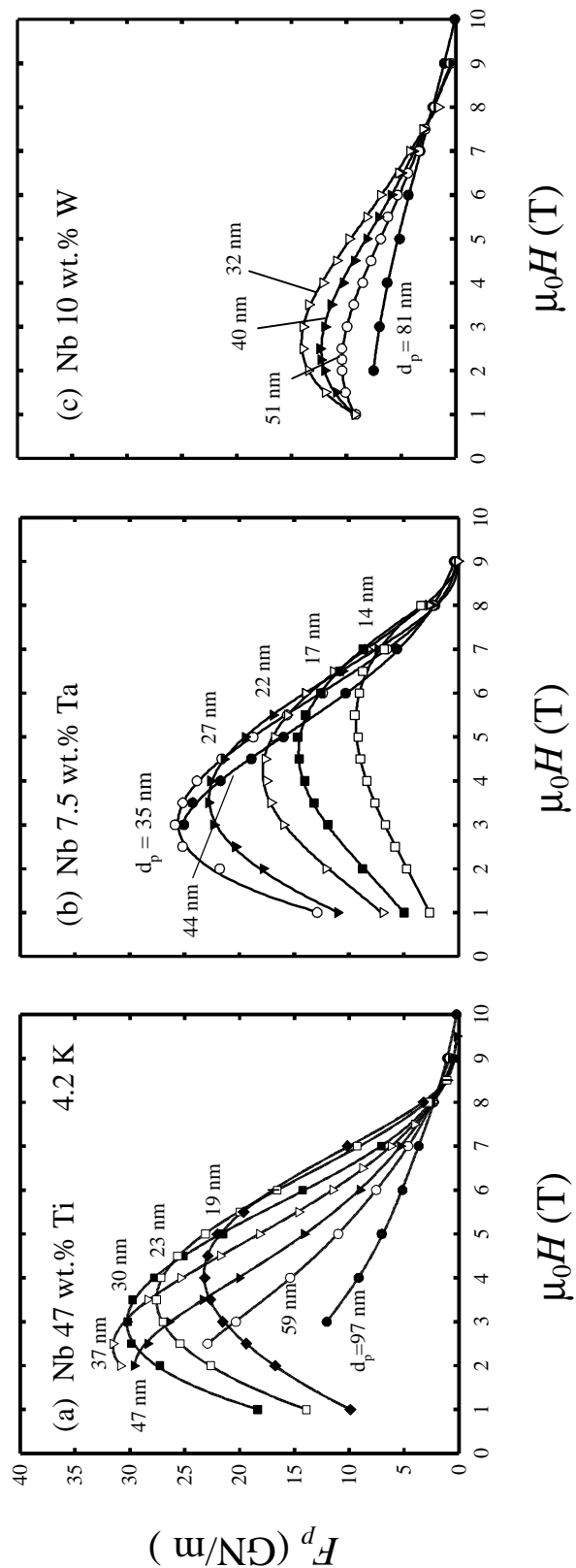
Figure 6.4: $F_p(H)$ as a function of $d_p$ for the (a) Nb, (b) Nb-Ta, and (c) Nb-W-pin composites at 4.2 K. Note that wires with $d_p < 32$ nm were not fabricated for the Nb-W-pin composite due to fabrication difficulties.

60% shorter, respectively, than that of pure Nb (83 nm). Nb 10 wt.% W has the same proximity length as found for pure Ti, but $x_N$ for $a$-Ti is likely even shorter because it is alloyed with ~5 at.% Nb [21].

The trends seen in the $F_p(H, d_p)$ curves of Figure 6.4 are qualitatively consistent with the magnetic pinning model. As the pin proximity length was reduced, the value of $h_{max}$ increased and $F_{pmax}$ occurred at smaller nominal pin diameters. Stronger validation of the magnetic pinning model may come with the identification of $h_{max}$ and $F_{pmax}$ in the Nb 10 wt.% W-pin composite, which unfortunately, was not possible in this study due to the fabrication difficulties discussed above.

APC fabrication improvements are still being made. Our earlier work on pure Nb-pin APC composites (chapter 4) produced large increases (~40%) in $F_{pmax}$ with little change in $h_{max}$. Nb 7.5 wt.% Ta is almost identical to Nb in hardness, work-hardening and fabricability. However, the Nb 10 wt.% W was markedly worse, undoubtedly because W has a smaller atomic radius (0.142 nm) than both Nb and Ta (0.147 nm), causing the increased work-hardening behavior shown in Figure 6.3. However, the 32 nm limit placed on the Nb 10 wt.% W pin diameter in this experiment should not be considered as a severe obstacle to fabricating wires with smaller nominal pin size. Composite fracture during the final extrusion may have been more a result of the billet design and extrusion parameters not being optimized for the higher overall Nb 47 wt.% Ti/Nb 10 wt.% W composite hardness, rather than as a direct consequence of the pin/matrix hardness disparity. This hypothesis is supported by the fact that the Nb 10

wt.% W-pin wire drew well following the final extrusion; the pin sausaging observed in Figure 6.2(c) did not adversely affect its ductility. Thus a key to improving composite fabricability in this particular case may lie in simple adjustments of one or more of the extrusion parameters. Predictive equations by Avitzur [59] suggest that making the Nb-Ti/Nb-W and matrix more similar by increasing the matrix flow stress (e.g. using Cu 30 wt.% Ni instead of Cu) or decreasing the copper-to-superconductor ratio are two means for promoting uniform composite deformation during extrusion. These modifications are easily implemented and indeed desirable because neither requires an increase in the extrusion temperature. New composites utilizing these design modifications are currently in manufacture.

## 6.4  Conclusions

Nb 47 wt.% Ti wires containing 25 vol.% of alloyed Nb pins were fabricated to evaluate the effect of the pin proximity length $x_N$ on the flux pinning properties. The proximity length of pure Nb, 83 nm, decreased to 59 nm and 32 nm when alloyed with 7.5 wt.% Ta and 10 wt.% W, respectively. The field and pin thickness dependence of $F_p$ qualitatively support the magnetic pinning model; as $x_N$ decreased, the field and pin thickness at which the maximum $F_p$ occurred increased and decreased, respectively. Excessive hardening of the Nb 10 wt.% W-pin composite, an adverse effect of the tungsten alloying addition, caused non-uniform composite deformation during the final extrusion and prevented wires with $d_p < 32$ nm from being fabricated.

# 7. Summary

Superconducting Nb-Ti wires containing uniform arrays of Nb artificial pinning centers were fabricated and their microstructures and electromagnetic properties characterized as the pin size and spacing were reduced to the nanometer dimensions of the flux line lattice. Through careful control of the thermomechanical treatment, the critical current density of a composite containing Nb 47 wt.% Ti with 24 volume percent of Nb pins was raised to 4600 A/mm$^2$ at the benchmark field (5 T) and temperature (4.2 K), thus establishing a new record for any round-wire of Nb-Ti. Maximum $J_c$(5 T) occurred for a nominal pin diameter ($d_p$) of 25 nm, but for which the actual pins were 1–15 nm thick elongated ribbons.

However, the high-field (>6 T) flux pinning in this Nb-pin wire was significantly lower than is achieved in conventional processed Nb-Ti, mainly because (1) $H_{c2}$ and $H*$

were depressed by ~1.5 T as compared to optimized, conventional Nb-Ti, and (2) $F_p(H)$ peaked at ~$0.3H_{c2}$ rather than at $0.5H_{c2}$ as is found for conventional Nb-Ti.

Two separate attempts were made to improve the high-field flux pinning of Nb-pin APC wires. The first attempt involved increasing the titanium content of the Nb-Ti matrix in order to raise both $H_{c2}$ and $H^*$ in the proximity-effect coupled limit (i.e. when the pin thickness is less than $\boldsymbol{x}$). A Nb 62 wt.% Ti-matrix composite, designed for maximum upper critical field in the coupled limit, exhibited an increased $H^*$ as the pin size was reduced. However, the enhancement was significantly less than predicted in the fully coupled limit, even when the pin thickness was much smaller than $\boldsymbol{x}$. In the context of existing proximity effect models, this can be attributed to the same minimal pin/matrix interdiffusion held responsible for high $J_c$ in the low to mid field range of 1–5 T.

A second attempt to improve the high field pinning involved decreasing the pin proximity length ($\boldsymbol{x}_N$) in order to shift the maximum in the bulk pinning force curve to higher field, in accordance with the magnetic pinning model of Cooley, Lee, and Larbalestier [52]. Through separate alloying additions of 7.5 wt.% Ta and 10 wt.% W the Nb-pin proximity length was reduced by 30% and 60%, respectively. The functional dependence of the bulk flux pinning force on $\boldsymbol{x}_N$, $d_p$, and $H$ agreed qualitatively with the magnetic pinning model. However, excessive hardening of the Nb-W-pin composite, an adverse effect of the tungsten alloying addition, caused non-uniform composite deformation during the final extrusion and prevented the full effect on $F_p(H, d_p)$ from being evaluated.

Finally, during the course of this thesis, a robust process for fabricating APC wires with large filament diameters and uniform pin arrays was developed. This process should be readily applicable to a wide variety of artificial pin materials. However, as illustrated by the Nb 10 wt.% W-pin composite, processing modifications will continually need to be made to accommodate pins with mechanical properties which differ significantly from those of the Nb-Ti matrix.

# Bibliography

[1]     F. London and H. London, Proc. Roy. Soc. (London) **A155**, 71 (1935).

[2]     A.B. Pippard, Physica **19**, 765 (1953).

[3]     V. Ginzburg and L. Landau, Zh. Eksperim. I Thor. Fiz. **20**, 1064 (1950).

[4]     A.C. Rose-Innes and E.H. Rhoderick, *Introduction to Superconductivity*, Pergamon Press, Oxford (1978).

[5]     W. Meissner and R. Ochsenfeld, Naturwissen **21**, 787 (1933).

[6]     A.A. Abrikosov, Soviet Physics JETP **5**, 1174 (1957).

[7]     A.M. Campbell and J.E. Evetts, Adv. Phys. **21**, 199 (1972).

[8]     E.J. Kramer and H.C. Freyhardt, J.Appl. Phys. **51**, 4930 (1980).

[9]     T. Matsushita, J. Appl. Phys. **54**, 281 (1983).

[10]    C. Meingast and D.C. Larbalestier, J. Appl. Phys. **66**, 5962 (1989).

[11]    G. Stejic, Ph.D. Thesis, University of Wisconsin–Madison (1993).

[12]   H. Ullmaier, *Irreversible Properties of Type-II Superconductors*, Springer-Verlag, Berlin (1975).

[13]   X.G. Qiu, S. Takahashi and M. Tachiki, Physica C **216**, 49 (1993).

[14]   W.E. Yetter, D.A. Thomas, and E.J. Kramer, Phil. Mag. B **46**, 523 (1982).

[15]   W. Fietz and W. Webb, Phys. Rev. **178**, 657 (1969).

[16]   D. Dew-Hughes, Phil. Mag. **55**, 459 (1987).

[17]   D.C. Larbalestier and A.W. West, Acta Met. **32**, 1871 (1984).

[18]   D.C. Larbalestier, A.W. West, W.L. Starch, W. Warnes, P.J. Lee, W.K. McDonald, P. O'Larey, K. Hemachalem, B. Zeitlin, R. Scanlan and C. Taylor, IEEE Trans. MAG. **21**, 269 (1985).

[19]   M.J. Buckett and D.C. Larbalestier, IEEE Trans. MAG. **23**, (1987).

[20]   Li Chengren and D.C. Larbalestier, Cryogenics **27**, 171 (1987).

[21]   P.J. Lee and D.C. Larbalestier, Acta Met. **35**, 2523 (1987).

[22]   P.J. Lee and D.C. Larbalestier, J. Mat. Sci. **23**, 3951 (1988).

[23]   C. Meingast, P.J. Lee and D.C. Larbalestier, J. Appl. Phys **66**, 5962 (1989).

[24]   P.J. Lee, J.C. McKinnell, and D.C. Larbalestier, Adv. Cryo. Engr. **36A**, 287 (1990).

[25]   G. Stejic, L.D. Cooley, R. Joynt, and D.C. Larbalestier, Supercond. Sci. Tech. **5**, S176 (1992).

[26]   G.L. Dorofejev, E.Y. Klimenko, S.V. Frolov, E.V. Nikulenkov, E.I. Plashkin, N.I Salunin, and V.Y. Filkin, Proceedings of the Ninth International Conference on Magnet Technology, Ed. By C. Marinucci and P. Weymuth (pub. Swiss Institute for Nuclear Research, Villigen, Switzerland) 564 (1985).

[27]   B.A. Zeitlin, M.S. Walker, and L.R. Motowidlo, United States Patent No. 4,803,310 (Jan. 7, 1989).

[28]  L.R. Motowidlo, H.C. Kanithi, and B.A. Zeitlin, Adv. Cryo. Eng. **36A**, 311 (1990).

[29]  L.D. Cooley, Ph.D. Thesis, University of Wisconsin–Madison (1992).

[30]  L.D. Cooley, P.J. Lee, D.C. Larbalestier, and P.M. O'Larey, Appl. Phys. Lett. **64**, 1298 (1994).

[31]  K. Matsumoto, Y.Tanaka, K. Yamafuji, K. Funaki, M. Iwakuma, and T. Matsushita, IEEE Trans Appl. Supercond. **3**, 1362 (1993).

[32]  K. Matsumoto, Y. Tanaka, K. Yamada, O. Miura, United States Patent No. 5,374,320 (Dec. 20, 1994).

[33]  K. Matsumoto, H. Takewaki, Y. Tanaka, O. Miura, K. Yamafuji, K. Funaki, M. Iwakuma, and T. Matsushita, Appl. Phys. Lett. **64**, 115 (1994).

[34]  J. Wong, M.K. Rudziak, D. W. Capone II, United States Patent No. 5,158,620 (Oct. 27, 1992); J. Wong, M.K. Rudziak, United States Patent No. 5,160,550 (Nov. 3, 1992); J. Wong, M.K. Rudziak, D. W. Capone II United States Patent No. 5,160,794 (Nov. 3, 1992); J. Wong, M.K. Rudziak, United States Patent No. 5,223,348 (June 29, 1993).

[35]  T. Wong, M. K. Rudziak, J.M. Seuntjens, and J. Wong, IEEE Trans. Appl. Supercond. **7**, 1126 (1996).

[36]  R.W. Heussner, P.D. Jablonski, and D.C. Larbalestier, proceedings of the Low Temperature Superconductor Workshop, Devil's Head, WI, Feb. 8–10 (1994).

[37]  N.D. Rizzo, S. Ling, J.D. McCambridge, D. Prober, L. R. Motowidlo and B.A. Zeitlin, proceedings of the Low Temperature Superconductor Workshop, Devil's

[38]  P.D. Jablonski and D.C. Larbalestier, United States Patent No. 5,226,947 (July 13, 1993).

[39]  P.D. Jablonski, Ph.D. Thesis, University of Wisconsin–Madison (1994).

[40]  P.D. Jablonski, P.J. Lee, and D.C. Larbalestier, Mat.Res. Soc. Symp. Proc. **351**, 455 (1994).

[41]   P.D. Jablonski, P.J. Lee, and D.C. Larbalestier, Appl. Phys. Lett. **65**, 767 (1994).

[42]   L.N. Cooper, Phys. Rev. Letters **6**, 89 (1961).

[43]   P.G. de Gennes, Rev. Mod. Phys. **36**, 255 (1964).

[44]   P.G. de Gennes, *Superconductivity of Metals and Alloys*, W.A. Benjamin, New York (1966).

[45]   N.R. Werthamer, Phys. Rev. **132**, 2440 (1963).

[46]   W. Silvert, J. Low Temp. Phys. **20**, 439 (1975).

[47]   H. Muller (unpublished).

[48]   L.R. Motowidlo, B.A. Zeitlin, M.S. Walker, and P Haldar, Appl. Phys Lett. **61** 991 (1992)

[49]   L.D. Cooley (unpublished).

[50]   L.D. Cooley, P.J. Lee, and D.C. Larbalestier, IEEE Trans. Mag. **27**, 1097 (1991).

[51]   A. Gurevich and L.D. Cooley, Phys. Rev. B **50**, 13563 (1994).

[52]   L.D. Cooley, P.J. Lee, and D.C. Larbalestier, Phys. Rev. B **53**, 6638 (1996).

[53]   L.D. Cooley, to appear Adv. Cryo. Eng. **42**, (1998).

[54]   R.W. Heussner, C.B. Nunes, P.D. Jablonski, P.J. Lee, and D.C. Larbalestier, J. Appl. Phys. **80**, 1640 (1996).

[55]   P.J. Lee, D.C. Larbalestier, and P.D. Jablonski, IEEE Trans. Appl. Supercond. **5**, 1701 (1995).

[56]   M.N. Wilson, *Superconducting Magnets*, Oxford Press, New York (1983).

[57]   N.D. Rizzo, Ph.D. Thesis, Yale University (1997).

[58]   B. Avitzur, Trans. ASME Eng. for Ind. **90**, 79 (1968).

[59]    B. Avitzur, *Handbook of Metal-Forming Processes*, John Wiley & Sons (1983).

[60]    B. Avitzur R. Wu, S. Talbert, and Y.T. Chou, Trans. ASME Eng. for Ind. **108**, 133 (1986).

[61]    B. Avitzur and W. Pachla, Trans. ASME Eng. for Ind. **108**, 295 (1986).

[62]    B. Avitzur and W. Pachla, Trans. ASME Eng. for Ind. **108**, 307 (1986).

[63]    E.W. Collings, *Applied Superconductivity, Metallurgy and Physics of Titanium Alloys*, Plenum Press, New York (1986).

[64]    T.H. Courtney, *Mechanical Behavior of Materials*, McGraw-Hill Publishing Company, New York (1990).

[65]    D.C. Larbalestier, P.J. Lee, and R.W. Samuel, Adv. Cryo. Eng. **32**, 715 (1986).

[66]    K. J. Faase, P.J. Lee, and D.C. Larbalestier, Adv. Cryo. Eng. **38**, 723 (1992).

[67]    W.H. Warnes and D.C. Larbalestier, Cryogenics **26**, 643 (1986).

[68]    W.H. Warnes, J. Appl. Phys. **63**, 1651 (1988).

[69]    Y.E. High, J.C. McKinnell, P.J. Lee and D.C. Larbalestier, Adv. Cryo. Eng. **38**, 647 (1992).

[70]    L. Kaufman and H. Bernstein, *Computer Calculations of Phase Diagrams*, Academic Press, New York (1970).

[71]    D.L. Moffat, Ph.D. Thesis, University of Wisconsin–Madison (1986).

[72]    A. Parekh, Undergraduate Senior Thesis, University of Wisconsin–Madison (1988).

[73]    Hydrostatic extrusion press manufactured by Naples Research and Manufacturing, Inc., Naples, FL.

[74]    F. J. Fuchs, United States Patent No. 4,751,058 (June 14, 1988).

[75]    E. Gregory, T.S. Kreilick, J. Wong, A.K. Gosh, and W.B. Sampson, Cryogenics **27**, 178 (1987).

[76]   Z. Guo, Ph.D. Thesis, Oregon State University (1994).

[77]   J.C. McKinnell, Ph.D. Thesis, University of Wisconsin–Madison (1990).

[78]   C.P. Bean, Rev. Mod. Phys. **36**, 31 (1964).

[79]   P.D. Jablonski (unpublished).

[80]   C.B. Nunes, R.W. Heussner, and D.C. Larbalestier, J. Appl. Phys. **80**, 1647 (1996).

[81]   C.B. Nunes, R.W. Heussner, and D.C. Larbalestier, IEEE Trans. Appl. Supercond. **7**, 1138 (1997).

[82]   M. Suenaga, A.K. Ghosh, Y. Xu, and D.O. Welch, Phys. Rev. Lett. **66**, 1777 (1991).

[83]   L.A. Bonney, T.C. Willis, and D.C. Larbalestier, J. Appl. Phys. **77**, 6377 (1995).

[84]   These data come from a 61-filament multifilamentary Nb 47 wt.% Ti composite fabricated at the University of Wisconsin–Madison Applied Superconductivity Center and designated CB9738.  The composite processing included $3 \times 80$ hr/420 $^{\circ}$C heat treatments.  It is among the highest $J_c$ multifilamentary Nb-Ti composites ever produced.

[85]   J.F. Peck and D.A. Thomas, Trans. Met. Soc. AIME **221**, 1240 (1961).

[86]   W.F. Hosford, Trans. Met. Soc. AIME **230**, 12 (1964).

[87]   J.C. Malzahn Kampe and T.H. Courtney, Scripta MET. **23**, 141 (1989).

[88]   R.W. Heussner, P.J. Lee, and D.C. Larbalestier, IEEE Trans. Appl. Supercond. **3**, 757 (1993).

[89]   R.W. Heussner, P.D. Jablonski, P.J. Lee, and D.C. Larbalestier, Adv. Cryo Eng. **40**, 755 (1994).

[90]   C.B. Nunes (unpublished).

[91]   L.R. Motowidlo, B.A. Zeitlin, M.S. Walker, P. Haldar, J.D. McCambridge, N.D. Rizzo, X.S. Ling, and D. E. Prober, IEEE Trans. Appl. Supercond. **3**, 1366 (1993).

[92]   H.C. Kanithi, P. Valaris, L.R. Motowidlo, B.A. Zeitlin, and R.M. Scanlan, Adv. Cryo. Eng. **38**, 675 (1992).

[93]   R.W. Heussner, C.B. Nunes, L.D. Cooley, and D.C. Larbalestier, IEEE Trans. Appl. Supercond. **7**, 1142 (1997).

[94]   O. Miura, K. Matsumoto, Y. Tanaka, K. Yamafuji, N. Harada, M Iwakuma, K. Funaki, and T. Matsushita, Cryogenics **32**, 315 (1992).

[95]   K. Matsumoto, Y. Tanaka, K. Yamafuji, K, Funaki, M. Iwakuma, and T. Matsushita, Supercond. Sci. Tech. **5**, 684 (1992).

[96]   D.C. Larbalestier and A. West, Acta Met. **32**, 1871 (1984).

[97]   J.D. McCambridge, N.D. Rizzo, X.S. Ling, J.Q. Wang, D.E. Prober, L.R. Motowidlo, and B.A Zeitlin, IEEE Trans. Appl. Supercond. **5**, 1697 (1995).

[98]   E. Kadyrov, A. Gurevich, and D.C. Larbalestier, Appl. Phys. Lett. **68**, 1567 (1996).

[99]   T. Matsushita and H. Küpfer, J. Appl. Phys. **63**, 5048 (1988).

[100]  M.T. Naus, R.W. Heussner, and D.C. Larbalestier, presented at the International Cryogenic Materials Conference, Portland, OR (1997).

[101]  N. Sato, J. Appl. Phys. **67**, 7493 (1990).

[102]  Y.J. Qian, J.Q. Zheng, B.K. Sarma, H.Q. Yang, J.B. Ketterson, and J.E. Hilliard, J. Low Temp. Phys. **49**, 279 (1982).

[103]  W.H. Warnes, K.J. Faase, and J.A. Norris, to appear Adv. Cryo. Eng. **42**, (1998).

[104]  K.J. Faase, Ph.D. Thesis, Oregon State University (1996).

[105]  M. Ledvij, L. Dobrosavljevic-Grujic, and J.R. Clem, Phys. Rev. B **38**, 129 (1988).

[106]  R.W. Heussner, P.D. Jablonski, P.J. Lee, and D.C. Larbalestier, IEEE Trans. Appl. Supercond. **5**, 1705 (1995).

[107]  D. Ohmann (unpublished).

[108]  J.A. Parrell, P.J. Lee, and D.C. Larbalestier, IEEE Trans. Appl. Supercond. **3**, 734 (1993).